Astron. Astrophys. 313, 65–90 (1996)

ASTRONOMY AND ASTROPHYSICS

Hydrodynamical simulations of the barred spiral galaxy NGC 1365

Dynamical interpretation of observations

P.A.B. Lindblad[1], **P.O. Lindblad**[1], **and E. Athanassoula**[2]

[1] Stockholm Observatory, S-133 36 Saltsjöbaden, Sweden
[2] Observatoire de Marseille, 2 Place Le Verrier, F-13248 Marseille Cedex 4, France

Received 7 July 1995 / Accepted 17 January 1996

Abstract. We perform two-dimensional, time dependent, hydrodynamical simulations of the gas flow in a potential representing the barred spiral galaxy NGC 1365 using the FS2 code originally written by G.D. van Albada.

Non-circular motions present in NGC 1365 prevent us from using an observed angle-averaged rotation curve as representative of the axisymmetric forces in the bar region. Comparing observed kinematics and gas features in NGC 1365 with corresponding quantities in the models enables us to estimate a possible representation of the true axisymmetric forces. We compute models perturbed by a pure bar potential and models perturbed by a bar + spiral potential.

A J-band image is used to estimate the bar potential under the assumption of a constant M/L_J ratio. The spiral potential is determined from the same image and has the same pattern speed as the bar, but is not assumed to have necessarily the same M/L_J ratio.

We find good agreement between observations and models, both concerning the H I and CO density distribution and the velocity field. Using just the shape of the observed bar potential we drive the main spiral features out to the required radius. Our best fitting bar model has a pattern speed of $\Omega_p = 20$ km s^{-1}kpc^{-1} placing corotation at a distance $R_{CR} \sim 145'' = 1.21 R_{bar}$, where R_{bar} is the optical semimajor axis of the bar. The offset dust lanes observed in optical images are reproduced by the models provided the latter have an inner Lindblad resonance at a radius of $\sim 27''$. Steep velocity gradients across the dust lanes and spiral arms are seen in both model and observations. Most observed features are reproduced in the models, and the general streaming motions are in qualitative agreement with linear gas orbit theory.

Contrary to observations, the pure bar perturbed models cannot drive an inner arm across corotation. Models having both a bar and spiral perturbing potential reduce this problem, thus suggesting the existence of massive spiral arms in NGC 1365. Our best fitting bar + spiral model has a pattern speed of $\Omega_p = 18$ km s^{-1}kpc^{-1} placing corotation at a distance $R_{CR} \sim 157'' = 1.31 R_{bar}$

Key words: galaxies: individual NGC 1365 – galaxies: kinematics and dynamics – hydrodynamics

Send offprint requests to: P.A.B. Lindblad, e-mail: pabli@astro.su.se

1. Introduction

1.1. Numerical simulations of barred spiral galaxies

Numerical N-body calculations, e.g. by Miller & Prendergast (1968), Hockney & Hohl (1969), Sellwood (1981), have shown that bars form naturally in rotationally supported discs, if the initial stellar disc is sufficiently cold, i.e. has small velocity dispersion, and if the relative mass of the stabilizing halo is low. As many of their observed properties resemble those of real bars, it seems likely that real bars are formed in a similar way (Sparke & Sellwood 1987).

Several authors have explored the field of gas dynamics in barred systems, using different approaches, numerical schemes and initial conditions. One of the aims of these investigations was to compare the model gaseous response, due to some assumed underlying stellar gravitational field, with observed gas density distribution and kinematics of barred galaxies. The gas is known to respond in a highly non-linear way, and therefore should give clues to dynamical parameters like the mass distribution, the positions and existence of principal resonances and thereby the pattern speed, which is the angular speed with which the bar rotates. The latter quantity is extremely difficult to obtain observationally, although attempts have been made using the method outlined by Tremaine and Weinberg (1984), e.g. Kent (1987), or using kinematical arguments, e.g. Jörsäter and van Moorsel (1995, hereafter JvM). Due to the large uncertainties in these methods, simulations are probably the best way to obtain an estimate of this evasive, but unfortunately very important, dynamical parameter.

Sanders & Huntley (1976) came to the conclusion that the natural response of any differentially rotating gaseous disc to an oval-like perturbation in an axisymmetric force field is to form a two-armed trailing spiral wave. The streamlines of the gas in their calculations are consistent with particle orbit theory in the epicyclic approximation far from resonances. Across the resonances the phase of the gas orbits changes smoothly, due to damping forces, in contrast to collisionless particles that show a discontinuous phase shift at the positions of the resonances. This conclusion was supported by Huntley et al. (1978), and the behaviour has been derived from linear gas orbit epicyclic theory independently by Lindblad & Lindblad (1994, hereafter LL94) and by Wada (1994). In the two latter papers the authors confirm the validity of the first order theory by comparison with numerical simulations.

Besides the gaseous spiral arms, one often observes in barred galaxies narrow offset dust lanes, situated at the leading edges of the bar (assuming trailing spiral arms). Prendergast (1962, unpublished) suggested that these features are due to shocks in the gas. Similar shocks show up quite naturally in gas dynamical calculations (e.g. Sørensen et al. 1976; Roberts et al. 1979; Sanders & Tubbs 1980; van Albada & Roberts 1981; Athanassoula 1992).

Athanassoula (1992) found that, in order for the shocks to be offset towards the leading side of the bar major axis, the x_2 family of orbits (in the notation of e.g. Contopoulos & Papayannopoulos 1980), oriented perpendicular to the bar major axis, must exist and have a sufficient extent, i.e. an inner Lindblad resonance (hereafter ILR) has to be present sufficiently far out in the galaxy model. She also finds that the Lagrangian radius has to lie in the interval $R_{\rm L} = (1.2 \pm 0.2)R_{\rm bar}$, where $R_{\rm bar}$ is the length of the bar semimajor axis.

Most papers mentioned so far treat the qualitative response of the gas to a bar, or oval perturbation, in order to compare the results with general observable features in barred galaxies. The potentials have either an analytical description or emanate from the results of N-body simulations. Even if these adopted potentials resemble the observed ones, it would be interesting to compare the results of a specific model, where the input parameters are taken as far as possible from the observations, with the system observed.

Sanders & Tubbs (1980) computed a grid of hydrodynamical models and compared their gaseous response with the gas morphology in the barred spiral galaxy NGC 5383, while Duval & Athanassoula (1983) estimated the M/L ratios of the various components in the surface density distribution of this galaxy by fitting the observed non-axisymmetric velocity field to hydrodynamical model velocity fields. Sempere et al. (1995a,b) estimated the pattern speeds of NGC 4321 and NGC 7479 by fitting models to observations.

Direct comparisons with the observed H I morphology and velocity fields have also been done for NGC 3992 (Hunter et al. 1988), NGC 1300 (England 1989), NGC 1073 (England et al. 1990) and NGC 3359 (Ball 1992). In these simulations the observed bar was used to constrain the mass distribution of the perturbation. Their major drawback is that they are not able to reproduce the observed spiral pattern without adding an *ad hoc* oval component to the model mass distribution in order to maintain the spiral response out to large radii.

The suggestion that the spiral arms could have a different pattern speed from that of the bar was brought up by Tagger et al. (1987), Sellwood & Sparke (1988) and Sygnet et al. (1988). In this case the two pattern speeds should be such that corotation (hereafter CR) of the bar should be in the same radial region as the ILR of the spiral (Tagger et al. 1987). In a later paper Sellwood & Wilkinson (1993) propose that the spiral arms in these galaxies do not result from forcing by the bar, but are different dynamical structures and that this could be the reason for the difficulties encountered when modeling the observed systems mentioned above.

1.2. The galaxy NGC 1365

NGC 1365 is one of the most thoroughly studied nearby isolated bright barred spiral galaxies. It is classified as being of type SBb(s) I-II by de Vaucouleurs et al. (1976), while Wright (1969) classified it as SBc(s) after rectifying the image. Assuming NGC 1365 to be associated with the Fornax cluster (Jones & Jones 1980) we adopt a distance of 20 Mpc (see also the discussion by Hjelm & Lindblad 1995)[1].

An optical IIIa-J plate of this galaxy, obtained by us at the prime focus of the ESO 3.6 m telescope, is reproduced in Fig. 1. There are several reasons to choose this galaxy for our hydrodynamical simulations. Besides the facts that it is relatively nearby and nearly bisymmetric in its appearance and lacks any obvious companion, it has an orientation in space favourable for kinematic and dynamical studies.

Kinematical data having a very complete coverage are now available for this galaxy. The velocity field in the intermediate and outer regions of NGC 1365, as obtained by high resolution H I observations with the VLA, has been presented by JvM. Optical long slit measurements, covering mainly the nucleus, bar and inner arm region have been presented by Jörsäter et al. (1984) and by Lindblad et al. (1996, hereafter L96). According to JvM, the outer disc in NGC 1365 shows a warped structure. This galaxy also contains a Seyfert 1.5 type nucleus and the optical spectra reveal a biconical nuclear high excitation outflow (Hjelm & Lindblad 1995).

The CO molecular gas is strongly concentrated to the nucleus and, further out, tends to be aligned with the dust lanes along the bar (Sandqvist et al. 1995).

An earlier investigation and modeling of the optical velocity field of the nuclear region of NGC 1365 was made by Teuben et al. (1986). These authors used the scanning Fabry-Perot interferometer TAURUS on the ESO 3.6 m telescope to observe the Hα velocity field. They found evidence for highly non-circular streaming motion consistent with an ILR at $R = 15''$ from the centre, which positions CR somewhat beyond the end of the bar ($100''$-$150''$). This, they conclude, is indicative of a pattern speed of approximately 25 km s^{-1}kpc^{-1}, but it could be as low

[1] The adopted distance gives a scale of $10'' = 1$ kpc.

as 15 km s^{-1}kpc^{-1} due to the depression of the $\Omega - \kappa/2$ curve by the strong perturbation.

The aim of the present paper is to compute the gas response to a model potential, obtained from a combination of a J-band image and the observed rotation curve of NGC 1365. We compute the response both for a bar, and for a bar + spiral perturbing potential. Our goal is to let the input parameters for the calculations be determined as far as possible by observations. The observations will of course also serve as the data set with which the morphological and kinematical results of the computations will be compared. A very similar approach is used to model the barred spiral galaxy NGC 1300 (Lindblad & Kristen 1996).

Wherever we mention radial positions of resonances, we refer to the value computed for nearly circular orbits using the adopted model input rotation curve. The discrepancy between these positions and those determined by periodic orbits will be largest for the inner resonances, i.e. the ILR and the inner 4 : 1 resonance, since the largest non-circular motions are found in the bar region.

2. Computational techniques

2.1. The FS2 code

We have chosen to use the numerical scheme FS2 (Flux-Splitting 2nd-order accurate) due to its low numerical viscosity and to its excellent performance in various tests (e.g. van Albada et al. 1982). This scheme was originally developed by G.D. van Albada, and a description of the code has been given by van Albada & Roberts (1981), van Albada et al. (1982) and van Albada (1985). The code solves the equations governing the flow of an ideal isothermal nonviscous gas in the frame of reference rotating with a given angular speed. These equations are

$$\frac{\partial \rho_g}{\partial t} + \nabla \cdot \rho_g \mathbf{u} = S(\rho_g, \mathbf{x}) \quad (1)$$

$$\frac{\partial (\rho_g \mathbf{u})}{\partial t} + (\nabla \cdot \rho_g \mathbf{u})\mathbf{u} + c_s^2 \nabla \rho_g = \rho_g \mathbf{A}(\mathbf{x}, \mathbf{u}) + \mathbf{u} S(\rho_g, \mathbf{x}) \quad (2)$$

where ρ_g is the gas density, $\mathbf{u}$ is the velocity, $\mathbf{x}$ is the position vector, c_s is the sound speed, S is a source term for the mass, and $\mathbf{A}$ is the acceleration, including the Coriolis and centrifugal forces due to the rotating frame of reference.

The fluid dynamical treatment of the interstellar medium is crude, but, as shown by Cowie (1980), it is not unreasonable to view the ensemble of cool clouds, present in the real galaxy, as a fluid with a sound speed of the order of the velocity dispersion of the clouds, i.e. typically 10 km s^{-1}.

The program requires an input potential described by a rotation curve, representing the axisymmetric part of the potential, and a perturbation (bar or bar + spiral) potential in the form of a Fourier series consisting of the cosine and sine $2\theta, 4\theta$ and 6θ -components, where θ is the azimuthal angle with respect to the bar major axis. The potential of the underlying stellar population is thus represented by the sum

$$\Phi(R,\theta) = \Phi_0(R) + \Phi_1(R)\sin 2\theta + \Phi_2(R)\cos 2\theta + \Phi_3(R)\sin 4\theta + \Phi_4(R)\cos 4\theta + \Phi_5(R)\sin 6\theta + \Phi_6(R)\cos 6\theta \quad (3)$$

For the pure bar case $\Phi_1(R)$, $\Phi_3(R)$ and $\Phi_5(R)$ are set to zero.

The version of the program we use here requires the galaxy model to be bisymmetric, and we carried out the calculations over half of the galaxy on Cartesian 80 × 160 or 160 × 320 grids, corresponding to a spatial resolution of 5″ and 2.5″ respectively.

For the initial gas surface density distribution we have chosen an exponential law of the form

$$\Sigma_{init}(R) = \Sigma_c \exp[-(R/R_0)^4] \quad (4)$$

where R is the radius from the centre in the plane of the galaxy and R_0 is determined by

$$R_0 = \frac{R_{max}}{(\ln(\Sigma_c/\Sigma_e))^{1/4}} \quad (5)$$

where R_{max} is the maximum radius of the grid. The surface density at the centre (Σ_c) and edge (Σ_e) are free parameters in the program. We have chosen this distribution since it has similar characteristics as the azimuthally averaged H I distribution in the outer parts $R > 100''$. In the inner $R < 50''$ the CO is highly peaked in contrast to our initial density distribution. We believe this to be an evolutionary effect, as is seen in our models showing strong gas concentrations in the central region.

The numerical viscosity, necessarily inherent in the code, depends on both the cell size, Δx, and the time step used, Δt, and should approach zero as $\Delta x, \Delta t \to 0$ with $\Delta x/\Delta t$ constant. The viscosity is also known to act in a similar way as a "real" viscosity (van Albada & Roberts 1981). The time step in our calculations is determined by the Courant condition which states that gas is not allowed to propagate a larger distance than Δx in one time step Δt. Thus a finer grid, and a necessarily smaller time step, imply a reduced numerical viscosity.

At the beginning of the simulations the gas is on circular orbits having the rotational velocities given by the input rotation curve. The velocities are adjusted for the pressure gradient caused by the gradient in the density distribution, thus the gas is initially in an equilibrium state. In order to avoid transients, the perturbing potential is introduced gradually, growing linearly during a period of 0.1 Gyr.

2.2. Tests of the code

The properties of the code have been tested extensively, both on one- and two-dimensional experiments. In the 1-D experiment described by van Albada et al. (1982), the low viscosity FS2 code had the best performance, of the codes tested, regarding the resolution of shocks. Also 1-D shock tubes, for which an exact time dependent solution can be derived, have been computed, and very good agreement with the exact solution was obtained here as well (van Albada 1985). As a 2-D test, we computed the evolution of the gas in a purely axisymmetric potential, starting from an equilibrium situation, and showed

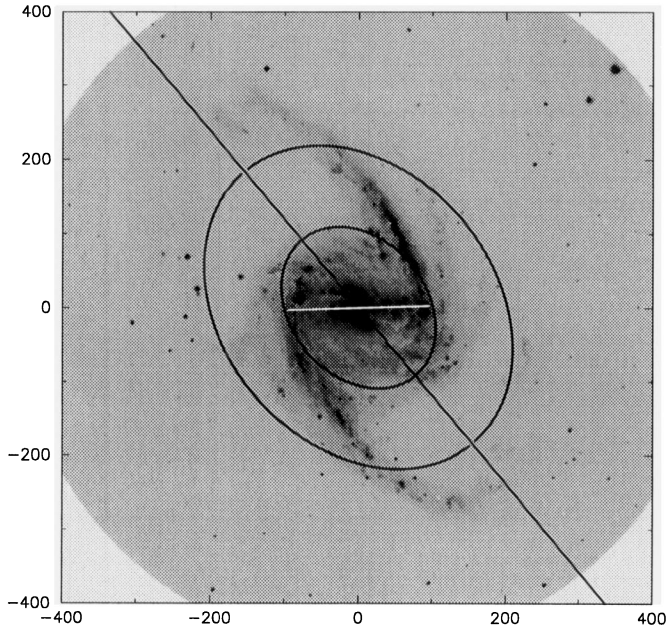

Fig. 1. A optical IIIa-J ESO 3.6 m prime focus plate of NGC 1365. The ellipses enclose the region $120'' < R < 240''$ where the rotation curve is believed to give a reliable description of the axisymmetric forces. Outside $R \sim 240''$ the disc is warped and inside $R \sim 120''$ the streaming motion is highly non-circular. The optical bar major axis and the line of nodes are marked as straight lines running through the centre

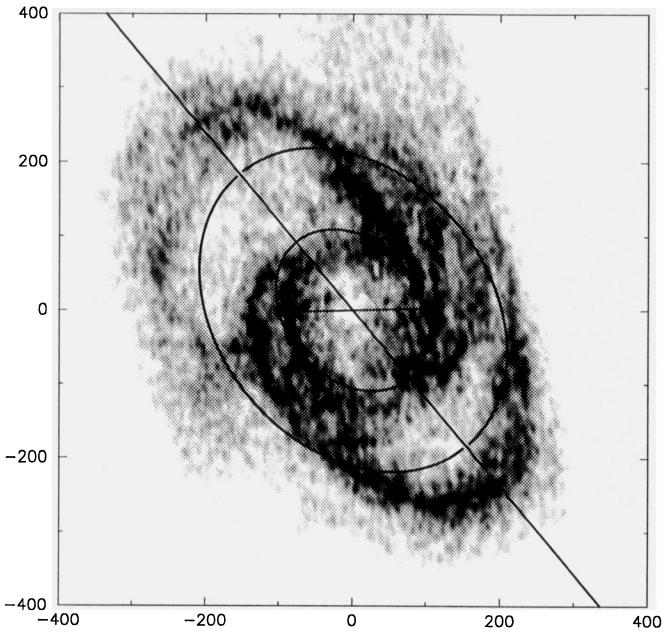

Fig. 2. The total H I column density map from JvM. The ellipses and lines are as defined in Fig. 1

that the gas stayed very close to the initial conditions. We also compared this code with analytic computations using the linear epicycle-approximation (see LL94). For weak bars, where the linear theory is valid, very good agreement between the results was found. This code has also been tested and used in a number of studies, e.g. by Athanassoula (1992).

As summarized by van Albada (1985), "FS2 is a reliable gas dynamics code for use in the study of galactic gas dynamics, given the assumption that the interstellar medium can be approximated by an isothermal perfect gas".

3. Observational data

We will here give a brief summary of the existing data used both to extract input parameters and for later comparison with models. The x- and y-axes of the images are centred on the position of the optical nucleus (Sandqvist et al. 1982) at $\alpha(1950.0) = 3^{\rm h}31^{\rm m}41\overset{\rm s}{.}80$, $\delta(1950.0) = -36°18'26\overset{''}{.}6$, and oriented so that North is up and West to the right. The spatial unit on all axis is arcseconds offset from the optical nuclear position.

3.1. Morphology

A IIIa-J plate of NGC 1365 is reproduced in Fig. 1. The "length of the bar", as defined later in connection with the bar potential estimate, is shown by the short line in position angle 92°.

JvM define a "standard region", namely an annulus in the plane of the galaxy in the radial range $120'' - 240''$, which is relatively undisturbed by the bar and not strongly affected by the warp. Within this region they derive a position angle for the line of nodes $PA_{\rm lon} = 220°$ and an inclination angle between the symmetry plane of the galaxy and the plane of the sky $i = 40°$ (we use an earlier estimate $i = 42°$ in the present investigation). The straight line in Fig. 1 having a position angle of $PA_{\rm lon} = 220°$ represents this line of nodes. The SW side of the galaxy is receding with respect to the nucleus, so the NW side is the near one (assuming trailing spiral arms).

The bar in NGC 1365 is strong, with prominent dust lanes running along its front edges. The spiral arms are well developed and have a tendency to turn inwards at the outer edge of the galaxy. Their structure appears at first look very symmetric. A closer look reveals multiple spiral arms and significant deviations from strict bisymmetry. In the optical inner disc, within about $100''$ from the centre, there is an intricate pattern of shorter spiral streaks, and the bar is crossed by a number of narrow dust lanes ending in the stronger dust lanes along the bar.

A mosaic image of NGC 1365 in the J-band was obtained by Jay Frogel at Las Campanas Observatory, and kindly put to our disposal by Alice Quillen[2]. The data were observed, reduced and combined into a mosaic (by J.A. Frogel and A. Quillen) identically to those of NGC 1097 as described by Quillen et al. (1995). More details will be given in upcoming releases of the survey (Frogel et al. 1995). The scale of the image was measured

[2] This image is part of the Ohio-State University Bright Galaxy Imaging Survey, which is being supported in part by NSF grant AST-9217716

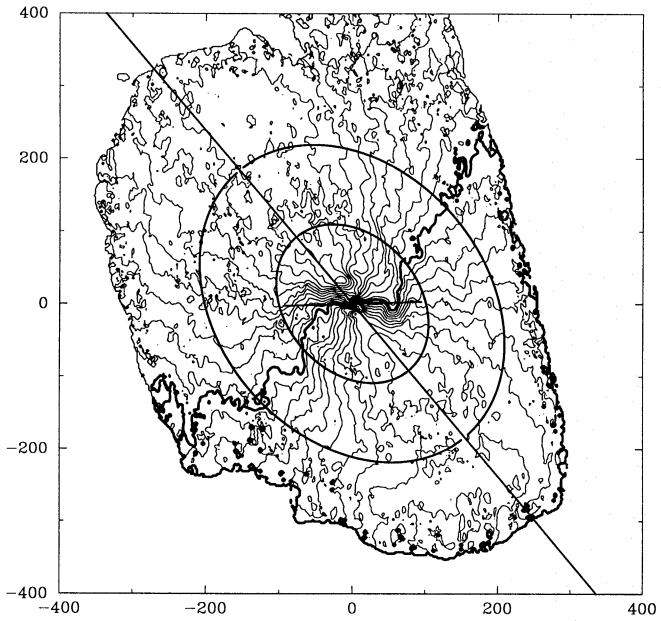

Fig. 3. The observed H I and optical hybrid radial velocity field, after subtraction of the systemic velocity, V_{sys} = +1630 km s^{-1}. The contour interval is 20 km s^{-1} and the zero radial velocity is marked by the thick contour. The ellipses and straight lines are as defined in Fig. 1

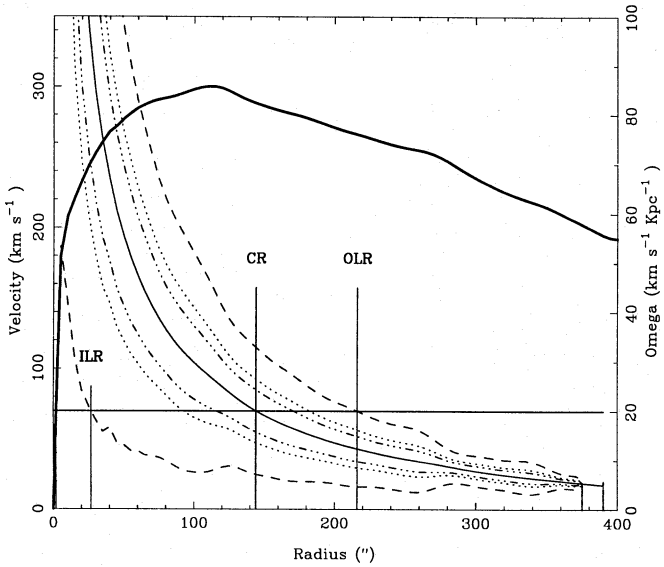

Fig. 4. The adopted rotation curve representing the axisymmetric forces in the models (thick line), and the corresponding Ω (solid), $\Omega \pm \kappa/2$ (dashed), $\Omega \pm \kappa/4$ (dotted) and $\Omega \pm \kappa/6$ (dash-dot). The positions of the main resonances are indicated where the straight horizontal line representing $\Omega = \Omega_p$ = 20 km s^{-1}kpc^{-1}, crosses the different curves

to be 0.″920/pix. The image was cleaned from bright foreground stars, and a background level was subtracted. Inclination correction was done, and the bar major axis was aligned with the x-axis. We show this image as a contour plot in Fig. 10a. It presents the structure of the bar and inner spiral arms almost unobscured by dust extinction. We will use this image to derive the gravitational potential of the bar and of the main spiral structure.

JvM have presented a very detailed study of NGC 1365 in the H I 21 cm line using the VLA in a number of different configurations. The spatial resolution in their final maps is $\sim 7''$ and the velocity increment between the channel maps is 20.8 km s^{-1}. The total H I column density map is reproduced in Fig. 2. H I is almost entirely absent from the bar region, with the exception of a few H II regions, mostly found in the dust lanes along the leading edges of the bar. In the nucleus H I is seen in absorption. The H I gas mass inside a radius of $R \sim 400''$ is estimated to $\sim 15 \times 10^9 M_\odot$, and the total mass of NGC 1365, as estimated from the rotation curve, is $\sim 3.9 \times 10^{11} M_\odot$ within the same radius.

The morphology of the H I total column density map differs in some respects from the impression given by the optical image. If we restrict ourselves to the SE side of the line of nodes, the H I gas has a strong double arm structure, the outer arm being much more dominant than in the optical image. This arm can be traced for at least 180°. The inner H I arm is parallel to the main arm out to a radius of approximately 140″, where it seems to split up in one part that turns inward and another that continues downward.

The optical image also reveals a double arm structure to the SE side of the line of nodes, where the bright inner optical arm, clearly dominant in terms of star formation, overlaps the inner H I arm inside 140″ and connects with the outer H I arm. The outer optical arm coincides with the outer H I main arm all the way.

The CO $J = 1 - 0$ and $J = 2 - 1$ transitions have been observed using the Swedish ESO Submillimeter Telescope (SEST) by Sandqvist et al. (1995). They find that CO is highly concentrated to the nuclear region, with weak extensions along the dust lanes on the leading side of the bar. The H_2 mass is estimated to $\sim 20 \times 10^9 M_\odot$, with $\sim 6.3 \times 10^9 M_\odot$ inside a projected radius of 2.2 kpc from the nucleus.

3.2. Radial velocities

The H I velocity field, derived by JvM, gives input kinematic data, in particular for the outer regions of the galaxy.

A total of 28 optical long slit spectra has been collected over the years, and the accumulated data is now being presented by L96. Even if the spatial coverage is necessarily rather poor, the spectra have been oriented in order to measure interesting features like shocks or velocity gradients across spiral arms and dust lanes, and are therefore very useful for comparison with similar model features.

Thus the observed velocity field in NGC 1365 is composed of two parts. In the outer region of the field, $R > 80''$, the radial velocities are from H I data, while in the inner region, $R < 80''$, they are obtained mainly by optical slit velocities. The two different fields are weighted together into a hybrid velocity field. The exact procedure for creating this hybrid velocity field is

described in detail in L96. In Fig. 3 we show this radial velocity field (see also Fig. 20a and b).

4. Input potential

4.1. Rotation curve and axisymmetric potential

In strongly nonaxisymmetric galaxies like NGC 1365 the azimuthally averaged observed rotation curve is not a good description of the underlying axisymmetric potential in the bar region (e.g. Fig. 16 of Duval and Athanassoula 1983). Furthermore, if the outer disc is warped, as is the case for NGC 1365, the outer parts of the rotation curve may be ill defined. Thus there is only an intermediate region in which the rotation curve can be safely used to calculate the axisymmetric forces.

The H I rotation curve, derived by JvM, is the basis for our input rotation curve for the region $120'' < R < 400''$. Thus the warp has been taken into account and our models have been projected onto the sky using the variable warp orientation parameters, $PA_{\rm lon}(R)$ and $i(R)$, as derived by JvM, with 2° added to $i(R)$ (see above).

Estimating the axisymmetric forces for $R < 120''$, i.e. the bar region, is more difficult, since the streaming is highly noncircular. We assume that NGC 1365 has fixed orientation parameters in this region, $PA_{\rm lon} = 220°$ and $i = 42°$.

Surface photometry does not give a good approximation to the rotation curve, i.e. the axisymmetric potential, in the bar and nuclear region primarily because of the unknown 3-dimensional shape of the bulge mass distribution and the strong IR excess in the nuclear region. Assuming the bar not to be contaminated by any IR excess we can compute the nonaxisymmetric potential with some confidence. The assumed thickness of the bar is not a crucial parameter since this can effectively be modeled by varying the relative bar potential amplitude $A_{\rm bar}$ (see Sect. 4.2.1).

To find the true rotation curve in the inner region we adopt the following procedure:
The model fit in the outer regions of the galaxy is relatively unaffected by the exact shape of the rotation curve in the bar region. Therefore, by fitting the main H I arms, which lie outside the bar region, we can obtain an estimate of the pattern speed. As discussed in Sect. 6.1, the best fit for the bar + disc model is obtained for a pattern speed of $\Omega_{\rm p} \sim 20$ km s^{-1}kpc^{-1}.

Using this value of the pattern speed, the existence and positions of offset dust lanes, and the velocities from slit spectra (L96) we choose the model input rotation curve in the bar region. The procedure of estimating the rotation curve was first to identify the possible location for an ILR resonance, justified both by the results of Athanassoula (1992) and by the observed velocity field in the central region which suggests orbits elongated perpendicular to the bar in the inner region and twisting when crossing the ILR to an orientation parallel to the bar (see Sect. 6.1.3 and Teuben et al. 1986).

By altering the numerical values for the model input rotation curve until the above velocity and morphological constraints were met, we obtained the inner part of the rotation curve presented, together with the Ω, $\Omega \pm \kappa/2$, $\Omega \pm \kappa/4$ and $\Omega \pm \kappa/6$ curves, in Fig. 4. The positions of the main resonances are indicated where the straight line $\Omega = \Omega_{\rm p} = 20$ km s^{-1}kpc^{-1} crosses the different curves.

The adopted rotation curve inside $R < 120''$ represents an estimate of a possible variation of the axisymmetric forces in the bar region, which is in agreement with the observed morphology and velocity field.

4.2. Bar and spiral potential

We will perform two different types of simulations: one where the perturbing potential arises from the bar only, and one where we include a spiral component. The second approach can be motivated by the J-band image which shows spiral arms, and it can also be seen as a first step towards self-gravitating hydrodynamical simulations, since our gas response from bar + disc models always shows gaseous spiral arms emanating from the ends of the bar (see Sect. 6.1.2).

The considerable amount of obscuring dust covering a large fraction of the bar is a severe problem when doing surface photometry of late type barred galaxies and deriving the shape of the bar. On the other hand, due to the relatively large gas and dust content, observations of gas morphology and velocity fields of late type systems are of higher quality than in the case of early type galaxies.

4.2.1. Scaling the perturbing potential

We rely on the observed rotation curve for the axisymmetric potential, while using the observed J-band surface brightness to extract the perturbing potential. Since there are two different origins for the potentials, the J-band image is not absolutely calibrated, and the $M/L_{\rm J}$ ratio is unknown, we need to couple the two different potentials in some way. Furthermore, we must make sure that no negative densities are present in the models when varying the bar and spiral strength while keeping the rotation curve fixed.

To obtain this coupling we will assume that the observed axisymmetric Fourier component of the J-band surface brightness, $\Sigma_0(R)$, represents the axisymmetric mass distribution giving the rotation curve in the radial interval $120'' < R < 200''$. This of course assumes that either the dark matter content in this region of NGC 1365 is low, which is in agreement with the conclusion of JvM, or that it is distributed as the visual matter, i.e. as the observed J-band surface brightness.

In Fig. 5 we present the fit between the observed H I rotation curve and the photometric rotation curve, computed using Eq. (A12) of Appendix A having $Z_0 = 1, 2, 3$ kpc respectively and the scale factor $M/L_{\rm J} = 6$ (in our arbitrary scale). As can be seen in Fig. 5, it turns out that the best fit, in the interval of R stated above, is not very sensitive to the value of Z_0. It is worth noting that we have, at this stage, assumed the bulge to be as flat as the disc. This should, however, not matter much in the radial interval under consideration. The comparison of the two rotation curves allows us to scale the perturbing surface brightness components into perturbing surface density components.

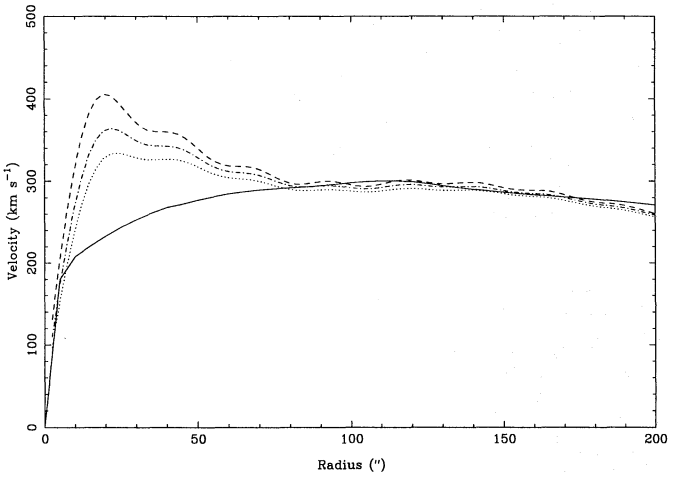

Fig. 5. The rotation curve from Fig. 4 (solid), together with photometric rotation curves assuming different values of Z_0 in Eq. (A12). The values are Z_0 = 1 (dashed), 2 (dash-dot), 3 (dotted) kpc respectively

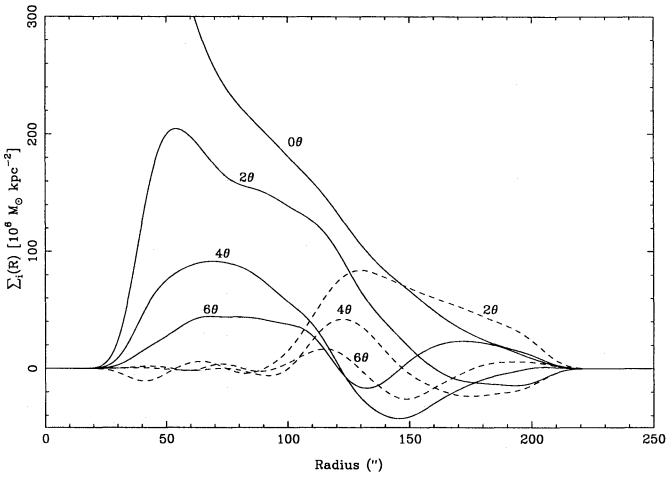

Fig. 7. The amplitudes of the cosine $0\theta, 2\theta, 4\theta, 6\theta$ (solid) and the sine $2\theta, 4\theta, 6\theta$ (dashed) surface density Fourier components obtained from the J-band image

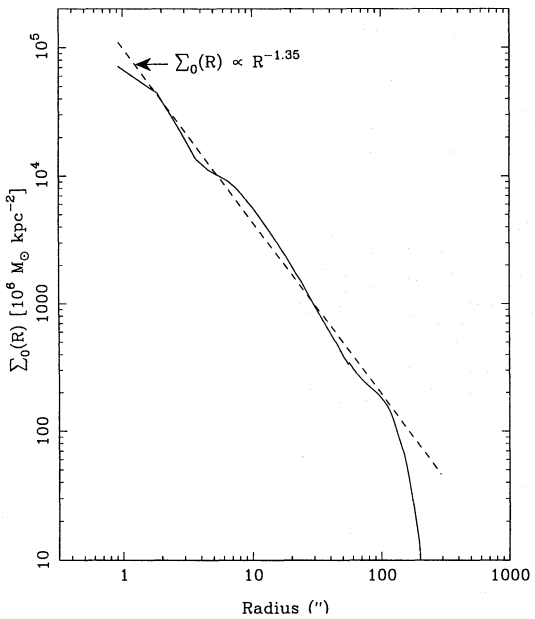

Fig. 6. Axisymmetric J-band surface density, $\Sigma_0(R)$ (solid) together with the function $\Sigma_0(R) \propto R^{-1.35}$ (dashed)

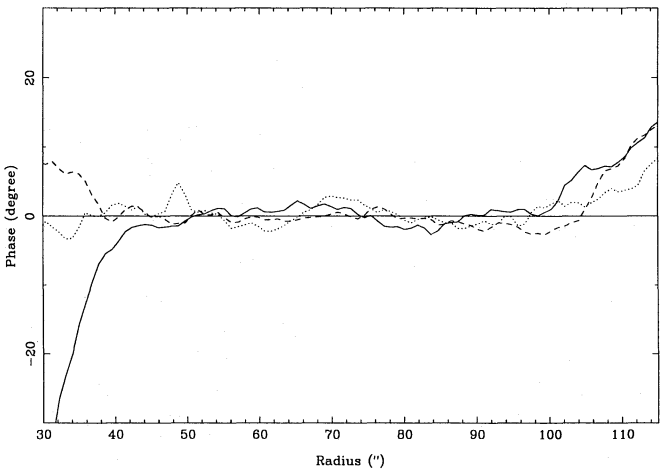

Fig. 8. The phase, in degrees, of the surface density 2θ (solid),4θ (dashed) and 6θ (dotted) Fourier components. The phase zero degrees, marked with the horizontal straight line, corresponds to the bar major axis

Applying the scale factor $M/L_J = 6$ gives us the axisymmetric surface density shown in Fig. 6. The axisymmetric surface density closely follows a power law, with index $\alpha = -1.35$, in the entire bar region. The same relation was also found to hold for the barred galaxy NGC 1300 (Lindblad & Kristen 1996). Whether this is a general characteristic of barred galaxies or not is, however, difficult to say on the basis of only two cases.

4.2.2. Bar + spiral surface density

The underlying stellar population is represented by the J-band surface brightness. At these wavelengths the dust is almost transparent, and no dust correction procedure in the *bar region* is necessary. However, in the *central region* the isophotes are clearly influenced by the dust and determining the underlying surface density is more difficult. We decomposed the J-band image into its surface brightness Fourier components and applied the $M/L_J = 6$ to obtain the surface density components shown in Fig. 7. The phases of these components are plotted in Fig. 8. The spatial limit of the J-band image is $R \sim 200''$, thus our Fourier components are artificially truncated at that radius. In order to avoid sharp gradients, we extrapolated the components out to $R \sim 220''$. Inside $R \sim 30''$ the isophotes were clearly influenced by dust absorption, therefore we have truncated and smoothed our surface density Fourier components within this

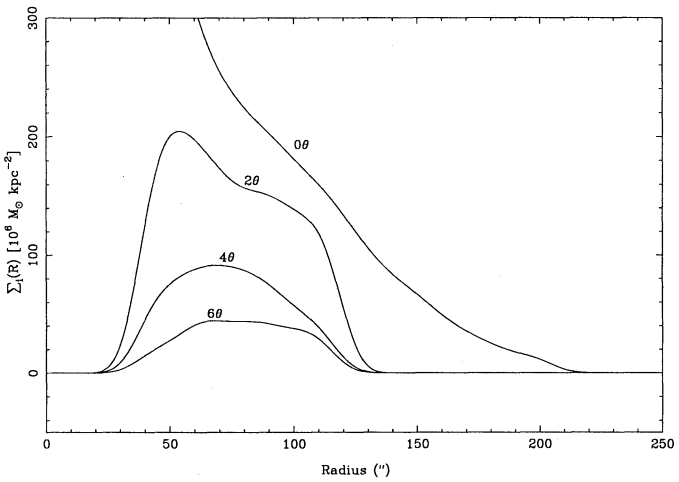

Fig. 9. Amplitude of the surface density cosine $0\theta, 2\theta, 4\theta, 6\theta$ Fourier components for the bar + disc model

radius, which gives us an axisymmetric surface density in the central parts.

4.2.3. Bar surface density and potential

When trying to isolate the bar surface density from the spiral arm component we have to estimate the radius where the bar ends, i.e. whether the outermost part of the "bar" is actually the beginning of the spiral arms or not. Looking at the phases of the even Fourier components in Fig. 8 we see that they start to increase systematically with increasing radius at $R \sim 100''$, from the value zero, defining the bar major axis. This is approximately the radius where the spiral features start to influence the phase and amplitude of the Fourier components. To obtain the final shape of the model bar we set all sine components equal to zero and the amplitudes of the $\cos 2\theta$, $\cos 4\theta$, and $\cos 6\theta$ to zero outside the radius $R = 110''$, and then smoothed these amplitudes to avoid a discontinuous cutoff. The effective bar radius $R_{\rm bar}$ was then defined to be the radius at which the surface density of the $\cos 2\theta$ component dropped to a value of $0.5 \times \Sigma_{110}$, where Σ_{110} is the surface density of the $\cos 2\theta$ component at the radius $R = 110''$, i.e. the radius where we truncated the components. We thereby obtained a value of $R_{\rm bar} = 120'' \pm 10'' = 12 \pm 1$ kpc, where the error of 1 kpc is due to the width of the bar-spiral arm transition region. The adopted model bar surface density components are plotted in Fig. 9.

In Fig. 10 we present, together with the inclination corrected observed J-band image (Fig. 10a), a bar + spiral + disc model surface density distribution obtained from the Fourier components in Fig. 7 (Fig. 10b), the residual image obtained when subtracting this model from the observed, inclination corrected J-band image (Fig. 10c), the bar + disc model surface density distribution obtained from the Fourier components in Fig. 9 (Fig. 10d), and the corresponding residual image (Fig. 10e). As can be seen, the large scale J-band surface density is well described by the Fourier components. For the bar + spiral + disc model significant residuals are only present in the spiral arms, due to bright H II regions, and in the centre, due to the presence of dust absorption and bright star forming regions. For the bar +disc model the residual image is dominated by the spiral arms outside $R \sim 120''$ and by the centre residuals.

Again using Eq. (A12) of Appendix A, we computed the corresponding bar potential from the bar surface density. We assume the bar to have a constant thickness of $Z_0 = 1$ kpc when performing this computation. The amplitude of the resulting Fourier components is shown in Fig. 11. In the hydrodynamical simulations we multiply these components with the free parameter $A_{\rm bar}$, thus allowing for differences in $M/L_{\rm J}$ between bulge + disc and the bar. An upper limit of $A_{\rm bar} = 1.40$ is set by the requirement that the total surface density, when keeping the axisymmetric component fixed (representing the fixed rotation curve) and varying the bar strength, should always be positive.

To test the effect of Z_0 we computed the potential from a bar having $Z_0 = 2.5$ kpc. When comparing this potential with the one for $Z_0 = 1.0$ kpc, shown in Fig. 11, we found that the ratio between the $m = 2$ components of the potentials is close to 0.85. The ratio between the corresponding $m = 4$ (and even more so $m = 6$) components is somewhat lower, i.e. $m = 4$ and 6 are somewhat more affected by a change in scale height than $m = 2$. The difference, however, is not big and we can say that varying the relative bar potential amplitude, $A_{\rm bar}$, can be seen alternatively as a variation of the bar strength or of the scale height of the bar. This statement is confirmed by model computations.

4.2.4. Spiral surface density and potential

The pure spiral surface density Fourier components can be obtained by subtracting the bar + disc Fourier components of Fig. 9 from the bar + disc + spiral Fourier components of Fig. 7. Assuming the galaxy to be thin at the radius of the spiral arms, we obtained the pure spiral potential from the equations in Appendix A using $Z_0 = 0.5$ kpc in Eq. (A12). The $M/L_{\rm J}$ ratio from the bar scaling was used here as well. The pure spiral potential amplitude obtained in this manner is multiplied by the free parameter $A_{\rm spiral}$. Since the $M/L_{\rm J}$ ratio in the spiral component can differ from the $M/L_{\rm J}$ ratio in the bar, we vary the value of $A_{\rm spiral}$ in our modeling. The final model perturbing potential is obtained by adding the pure bar potential, with the amplitude scaled by $A_{\rm bar}$, to the pure spiral potential having the amplitude scaled by $A_{\rm bar} \times A_{\rm spiral}$.

5. Models

An advantage of using observations as far as possible to describe the (assumed) equilibrium state of the galaxy's mass distribution is that the number of parameters to explore is reduced to a minimum.

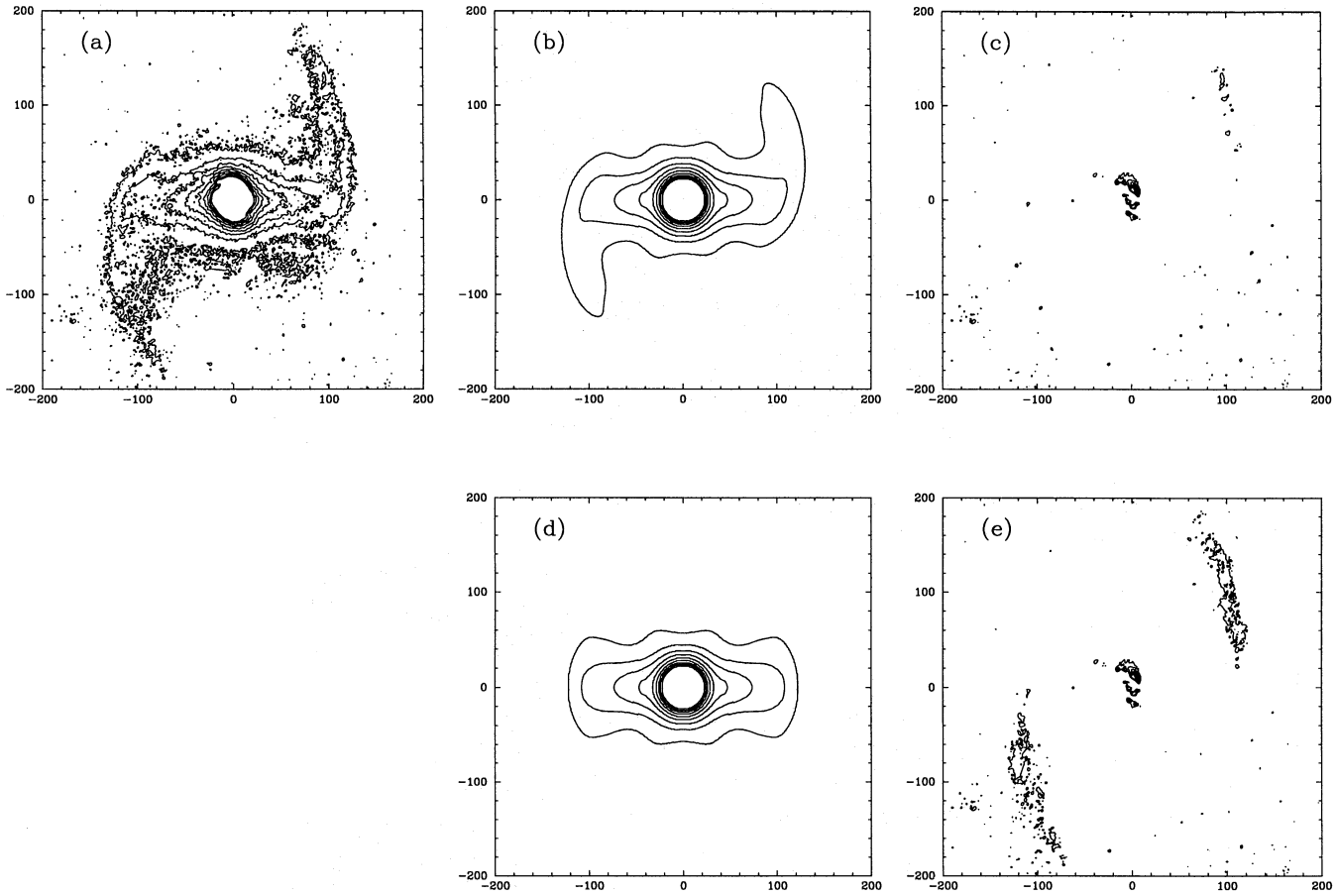

Fig. 10. **a** Inclination corrected J-band image, **b** bar + spiral + disc galaxy model obtained by the cos 0θ and the sine and cosine $2\theta, 4\theta$ and 6θ components in Fig. 7, **c** the corresponding residual image, **d** bar + disc galaxy model obtained by the cosine $0\theta, 2\theta, 4\theta$ and 6θ components in Fig. 9, **e** the corresponding residual image. The contour levels are from 180 to 1800 $10^6 M_\odot$ kpc^{-2}, with equal linear steps in surface density of 180 $10^6 M_\odot$ kpc^{-2}, and the same in all figures

5.1. Parameters

Parameters which have a large effect on the final gas response are called *free parameters* and these parameters are varied during the search for a best fit model. Parameters with only minor influence on the results (mostly regarding the final contrast between arm and interarm regions) are called *locked parameters*, and have, unless otherwise stated, their default values (mentioned below) in all models presented here.

5.1.1. Free parameters

The three free parameters in the models are:

1. The pattern speed Ω_p. This value controls the positions of the resonances and thus much of the model gas response. We have chosen to take as initial estimate of the pattern speed a value that puts CR just outside the end of the bar, in good agreement with what is known from numerical simulations (e.g. Sellwood 1981, Combes & Sanders 1981, Little & Carlberg 1991, Athanassoula 1992). We varied the pattern speed between $15 < \Omega_p < 23$ km s^{-1}kpc^{-1}, with a step of 1 km s^{-1}kpc^{-1} corresponding to a radial interval for the CR radius of $1.07R_{\rm bar} < R_{\rm CR} < 1.53R_{\rm bar}$.

2. The relative bar amplitude $A_{\rm bar}$. The value of $A_{\rm bar} = 1.0$ was derived by scaling surface photometry to the observed rotation curve, and should be taken as a guide to possible values. We varied this parameter between $0.0 < A_{\rm bar} < 1.4$ with a step of 0.2.

3. The relative spiral potential strength $A_{\rm spiral}$. This value was varied between $0.0 < A_{\rm spiral} < 1.0$ with a step of 0.1. The value $A_{\rm spiral} = 1.0$ is the spiral potential amplitude assuming the $M/L_{\rm J}$-ratio is the same in both the bar and spiral feature.

A coarse search through the above parameter space was done in order to locate the interesting region where models resemble the observations. The full 3-D parameter space, for the free parameters, was explored in the interval $16 < \Omega_p < 21$ km s^{-1}kpc^{-1}, $0.8 < A_{\rm bar} < 1.4$ and $0.0 < A_{\rm spiral} < 1.0$ during the search for best fit models.

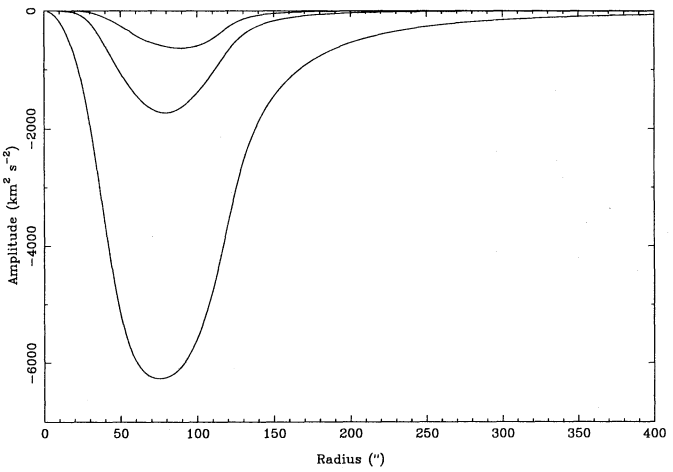

Fig. 11. Bar potential Fourier components corresponding to the relative bar potential strength $A_{\rm bar}$ = 1.0

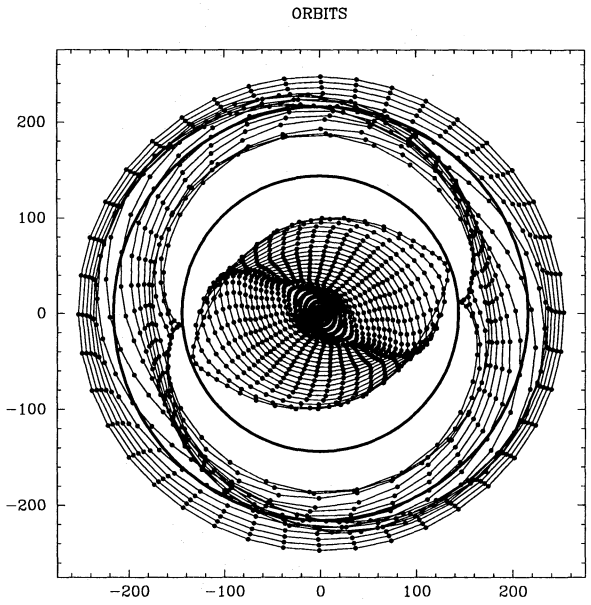

Fig. 12. Closed orbits for gas calculated in the linear epicycle approximation. The orbits gradually twist over the ILR and OLR. The axisymmetric forces are determined from the rotation curve in Fig. 4, and the major resonance positions are indicated by the circles. The bar perturbing forces are the same as in model BM (see Sect. 6.1). The bar major axis is horizontal and the direction of rotation is clockwise. The dots mark equal time intervals in the motion along the orbit

5.1.2. Locked parameters

The locked parameters in the models are:

1. The sound speed $c_{\rm s}$. The sound speed has, in this context, the meaning of a typical value of the velocity dispersion for interstellar clouds. The gas response is not very sensitive to this parameter, within reasonable limits, and $c_{\rm s}$ has been given the value 10 km s^{-1} in all the models presented here.

2. The growth time for the perturbation $T_{\rm grow}$. The perturbing potential grows linearly from zero to its final maximum amplitude during the time $T_{\rm grow}$. We use the value $T_{\rm grow}$ = 0.1 Gyr in all our models, which is found to be sufficient to avoid transients due to a rapid growth of the perturbing potential. One bar rotation is completed in 0.3 Gyr for a pattern speed of $\Omega_{\rm p}$ = 20 km s^{-1}kpc^{-1}

3. The gas density parameters Σ_c and Σ_e. The initial gas density distribution is described by Eqs. (4) and (5). The edge value Σ_e is set to a very low value to avoid instabilities developing at the border due to steep density gradients. The actual values of the edge and centre densities are not important in this context, since they can be normalized without affecting Eqs. (1) or (2), if self-gravity of the gas is neglected. We use the value $\Sigma_{\rm e}$ = 0.0006 $M_\odot$pc^{-2}, and the central value $\Sigma_{\rm c}$ = 6.0 $M_\odot$pc^{-2}.

5.2. Computations using linear epicyclic theory

In order to introduce a basic concept often referred to in the remaining part of this paper, we show here the principle of twisting orbits, illustrated in Fig. 12, where gas orbits, closed in a frame rotating with the pattern speed, have been calculated in the linear epicycle approximation (LL94) using the rotation curve and pure bar perturbation derived in Sect. 4. The input parameters are identical to that of model BM (see Sect. 6.1). The program that computes the orbits cannot handle the vicinity of CR, thus we do not present orbits in this region. Inside $R \sim 10''$ the orbits are slightly elongated approximately perpendicular to the bar major axis. Outside that radius they soon begin to twist counter-clockwise as they approach the ILR at $R \sim 27''$. This twisting and increasing elongation causes strong crowding of orbits and increased density on the leading side of the bar. Just outside CR the orbits are oriented perpendicular to bar major axis and have the shape of an "8" with the waist aligned with the bar major axis. The orbit orientation changes when crossing the outer Lindblad resonance (hereafter OLR) region towards being parallel to the bar outside the OLR. This gradual twist causes orbit crowding, outlining outer trailing spiral arms extending from CR to outside the OLR.

5.3. Modeling NGC 1365

The selection of a successful model of NGC 1365 is based on the following requirements:

1. The double armed H I morphology and the observed CO distribution, as well as the relative lack of gas, *both* atomic H I and molecular CO, between $50'' < R < 100''$ should be reproduced.
2. The offset gas lanes in the model should approximately have the same shape and position as the offset dust lanes observed in the real galaxy.

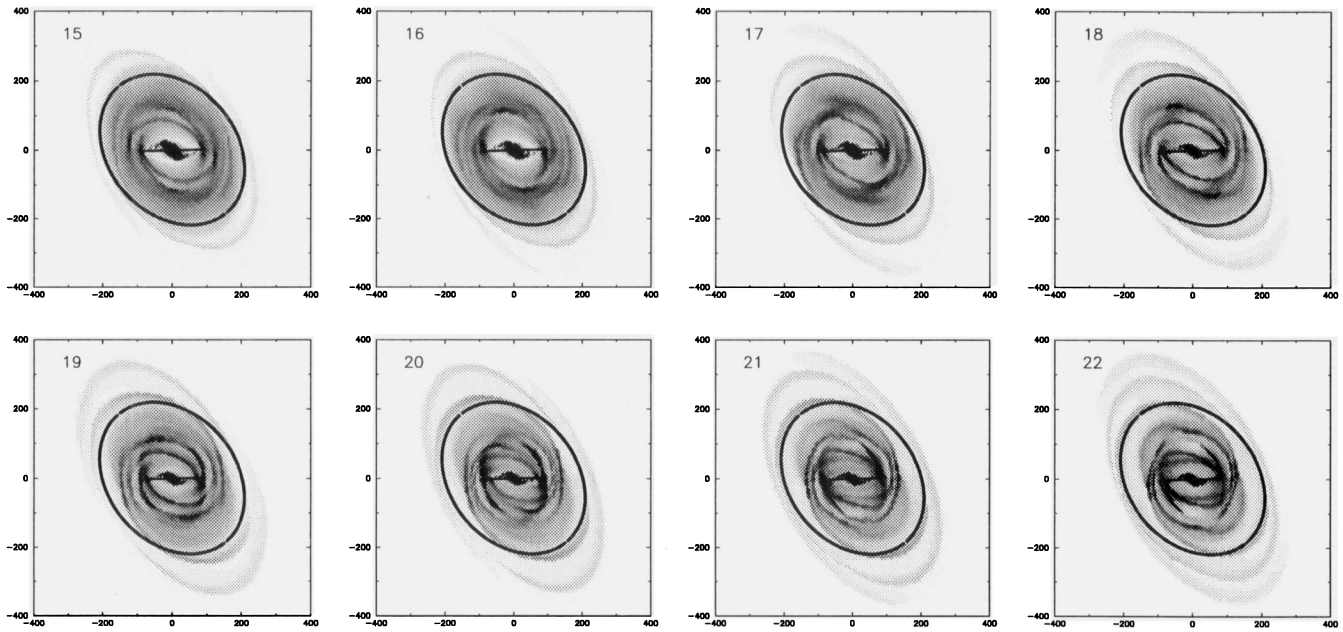

Fig. 13. Bar + disc models with different pattern speeds. The pattern speed was varied over $15 < \Omega_p < 22$ km s^{-1}kpc^{-1} in steps of 1 km s^{-1}kpc^{-1}, starting with $\Omega_p = 15$ in the upper left corner. The value of the pattern speed is given in the upper left corner of each panel. $A_{bar} = 1.2$ for all the models above. The ellipse marks the radius $R = 240''$.The straight line through the centre marks the position of the bar major axis

3. The model slit velocities, in the same positions as the observed ones, should have the same general trend as the observed ones. When the slits probe similar features, e.g. gas/dust lanes, spiral arms, in both NGC 1365 and the model, a detailed comparison helps to increase the viability of the model.
4. The gross characteristics and non-circular velocities in the observed H I velocity field should be reproduced.

In spite of its regular appearance NGC 1365 is clearly not strictly bisymmetrical, which our models are forced to be. Thus we will often concentrate our comparisons to the SE and S side of the galaxy that looks somewhat more regular.

We do not use any quantitative method, e.g. χ^2, to judge our models, since this could be misleading if strong density features or steep velocity gradients present in the models do not exactly overlap their observed counterparts. We judge our models by visual inspection of model density contour maps overlaid on the observed density counterpart, i.e. the H I total column density map in the outer regions and the optical B map in the bar region. We also judge our models by comparing model and observed non-circular motions in the form of residual maps, where the rotational component has been subtracted. We believe these comparisons to be sufficient in the context of our simple model.

5.4. Computed models

The models were run on a $800'' \times 800''$ frame, which corresponds to a cell size in the grid of $5''$ (160×160 grid), and evolved until a quasi-stationary steady state is reached, which takes about 1 Gyr for a typical model. Models evolved for a longer time only show a slow decrease in contrast due to the transparent outer boundary, and a continuous mass increase in the central region. The main characteristics of the gaseous response remain intact for at least 10 bar revolutions, where we halted the computations, corresponding to $\sim$ 3 Gyrs for a pattern speed of 20 km s^{-1}kpc^{-1}.

Most of the computed models were clearly incompatible with observations both concerning morphology and velocity field. In Figs. 13 and 14 we present cuts through the parameter space for the pure bar perturbed models where one of the parameters Ω_p or A_{bar} is held fixed, while the other is varied. The models have been projected to the same orientation as NGC 1365, with the warp taken into consideration. Models with a bar + spiral perturbation will be discussed in a subsequent section, thus $A_{spiral} = 0$ here.

Fig. 13 shows the gas response of models with pattern speeds varied over $15 < \Omega_p < 22$ km s^{-1}kpc^{-1} while the bar potential amplitude was fixed at a value of $A_{bar} = 1.2$. Since the rotation curve in the bar region was already derived on the basis of a pattern speed of $\Omega_p = 20$ (see Sect. 4.1), we should for the moment discard the bar region and focus our attention on the region in the radial interval $120'' < R < 240''$ where the H I rotation curve is a reliable measure of the axisymmetric forces in the plane. We see that the radial extent of the outer spiral feature depends strongly on the pattern speed, with a tighter wound response for a larger value of the pattern speed.

In Fig. 14 we present models having a fixed pattern speed of 20 km s^{-1}kpc^{-1} and where we varied the bar potential amplitude over $0.0 < A_{bar} < 1.4$. For $A_{bar} = 0.0$ the model stays

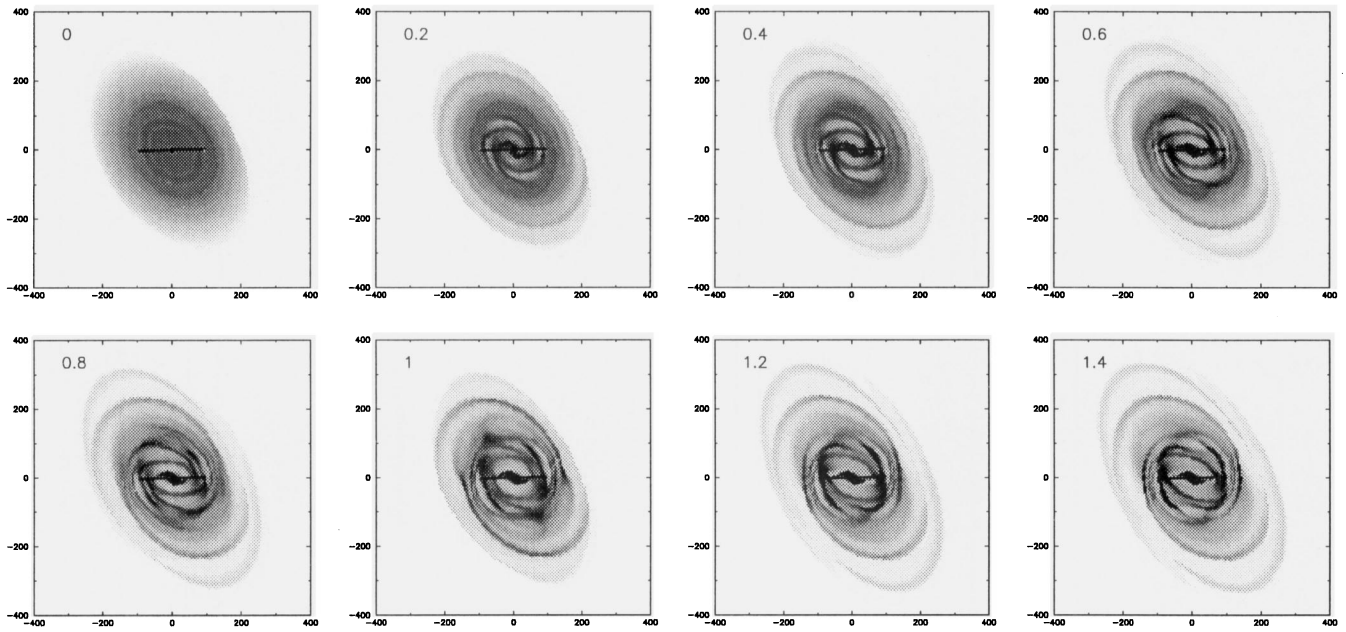

Fig. 14. Bar + disc models with different bar potential amplitudes. The amplitude was varied between $0.0 < A_{\rm bar} < 1.4$ with a step of 0.2, and starting with $A_{\rm bar} = 0.0$ in the upper left corner. The value of the pattern speed is 20 km s^{-1}kpc^{-1}. The value of $A_{\rm bar}$ is indicated in the upper left corner of each panel. The straight line through the centre marks the position of the bar major axis

close to the initial conditions, as expected. The extent of the spiral arms is not much affected by altering the bar potential, which is consistent with the idea that their extent is set by the resonances. The main influence of the parameter $A_{\rm bar}$ is to control the magnitude of the non-circular motions.

We recomputed our best fit models on a finer grid, thus with lower numerical viscosity, with a resolution of 2.″5 (320 × 320 grid) and found no differences except for sharper shock fronts due to the higher resolution. The results are thus *not* sensitive to the numerical viscosity inherent in the code for the grid sizes we used here. We have chosen the 160 × 160 grid since the spiral arms in the models then have a width similar to that of the H I arms observed.

We analyze and present models with just a perturbing bar potential in Sect. 6.1 and models having both a bar and spiral perturbation in Sect. 6.2. We also discuss models with different rotation curves in the outer region, depending on whether a warp is fully taken into consideration or not, in Sect. 6.3. We discuss the influence of gas self-gravity on our best fit models in Sect. 6.4, and star formation in Sect. 6.5.

6. Results

6.1. A bar + disc model; BM

We will here present what we consider to be a rather successful bar + disc model, hereafter BM. The reasons for selecting this model are the following: Fitting the main spiral arms in the models to the observed main H I arms (Fig. 2), gives us a pattern speed of 20 ± 1 km s^{-1}kpc^{-1}. A larger pattern speed gives a too tightly wound spiral response, while a lower value gives a too open response within the interval $120'' < R < 240''$ compared to NGC 1365.

Comparisons between model velocities and observed optical velocities along the minor axis of the galaxy point at bar potential amplitudes between $0.6 < A_{\rm bar} < 1.2$. Morphological comparisons favour $A_{\rm bar} = 1.0 \pm 0.2$ due to both the strong inner pair of arms, resembling the inner H I arms, and the well defined outer arms, to be compared with the observed main outer H I arms.

The model BM has a pattern speed of $\Omega_{\rm p} = 20$ km s^{-1}kpc^{-1} giving the main resonance radii $R_{\rm ILR} = 27''$, $R_{\rm CR} = 145'' = 1.21 R_{\rm bar}$, and $R_{\rm OLR} = 216''$. We have chosen a relative bar amplitude of $A_{\rm bar} = 1.2$. The spiral potential amplitude is set to $A_{\rm spiral} = 0.0$. The values of the locked parameters are the default values given in Sect. 5.1.2, and the axisymmetric forces in the model are represented by the adopted rotation curve plotted in Fig. 4.

6.1.1. Outer arms and CR

In Fig. 15a and b we see the gas response of BM, as a contour plot, overlaid both on the gray scale H I total column density map, and on the optical IIIa-J image. The outer SW H I arm is well fitted by the model out to a radius of $\sim 240''$. The fit to the NE H I arm is of lesser quality, but still acceptable. Outside this radius the model arms bend inwards earlier than the H I arms. The discrepancy can be explained in terms of the warped disc, which makes the determination of the observed apparent rotation curve somewhat uncertain here, and also complicates the projection of a model to the same orientation as NGC 1365. A

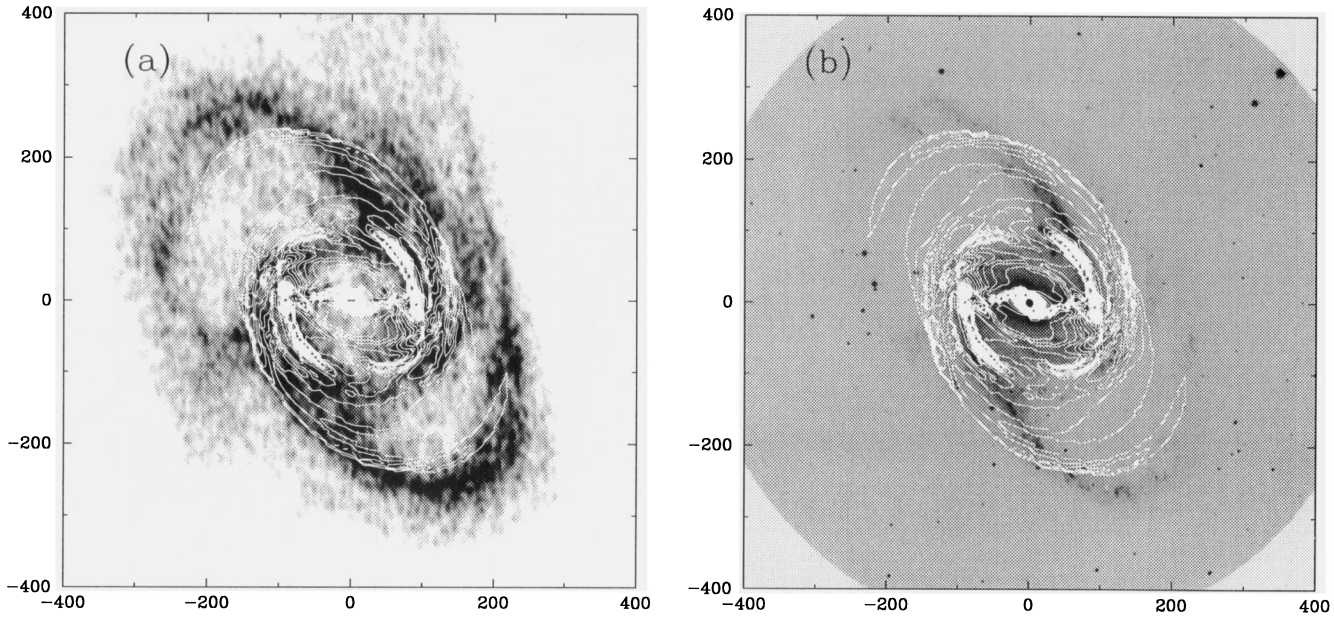

Fig. 15a and b. The BM density contour map overlaid on the total column H I density map (**a**), and the optical map (**b**). The straight line through the centre marks the position and length of the model bar major axis

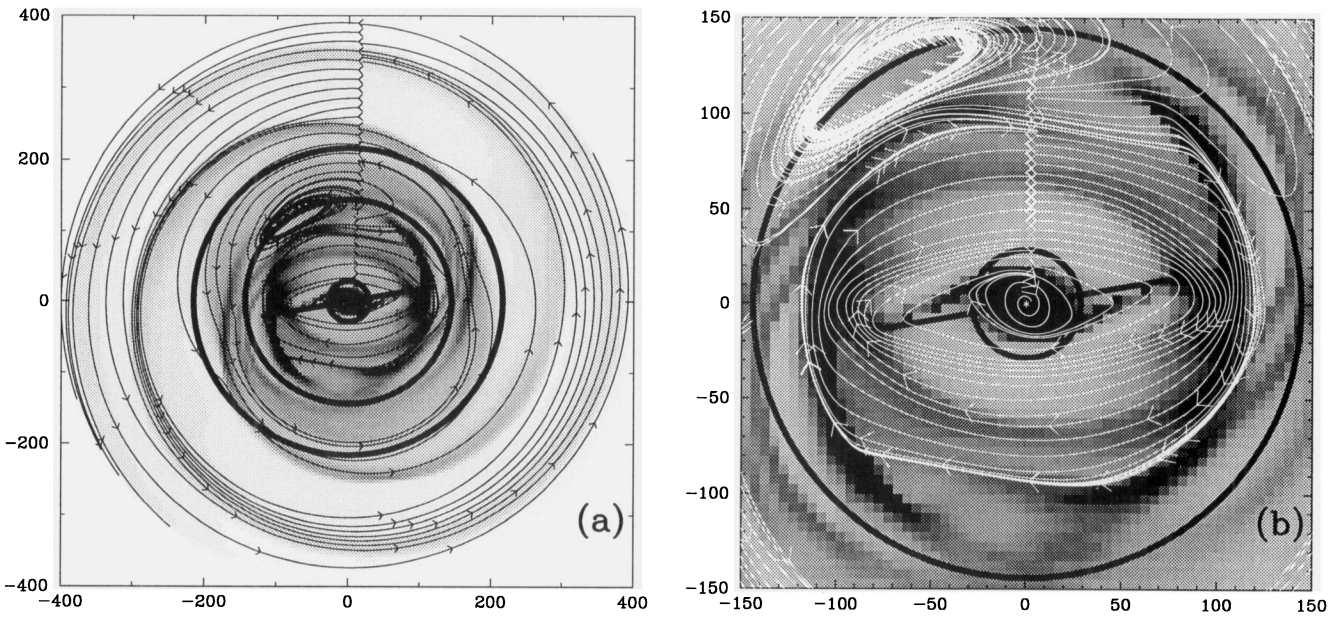

Fig. 16a and b. Gas flow lines from BM overlaid on gray scale maps of BM. **a** Full scale, **b** bar region. The model is seen face-on and the bar major axis is indicated by a straight line. The circles mark the ILR, CR and OLR resonance positions

perfect fit outside 240″ is thus not considered necessary for the model to be accepted.

In Fig. 16 we present the flow pattern in BM, on two different scales, overlaid on the face-on gray scale map of the gas density response in model BM. The flow lines trace the face-on flow of particles starting from a line in a position angle of 0°, and plotted in the reference frame corotating with the bar.

Orbits inside CR, sufficiently far from both CR and ILR, are oriented parallel to the bar major axis. When approaching CR the situation becomes more complex with "banana" orbits circling the Lagrangian points. The outer model arms form just outside CR, where the orbit orientation has become perpendicular to the bar major axis, and start to twist towards being parallel to the bar major axis when outside the OLR. This twisting is responsible

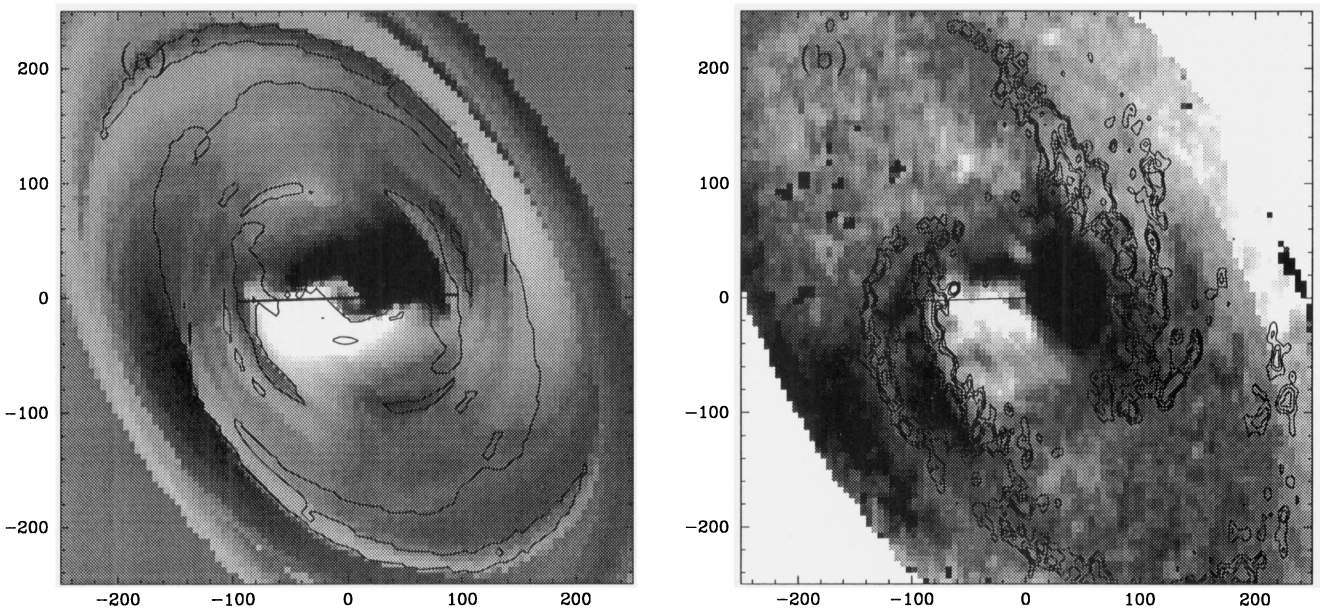

Fig. 17a and b. Velocity residual maps, after subtraction of the projected rotation curve, with density contour overlays: **a** for the bar + disc model BM, **b** for observations. Light shading indicates positive residual velocities and dark negative, in a scale that ranges from -40 km s^{-1} (black) to +40 km s^{-1} (white). The NW side of the galaxy is the near one

for the orbit crowding outlining the outer arms in BM (see also Fig. 12).

Residual velocity maps were created by subtracting a field of circular velocities corresponding to the adopted rotation curve shown in Fig. 4, projected onto the line of sight, from the model radial velocities and from the observed radial velocities respectively. In Fig. 17 we show these velocity residual maps with density contours overlaid, representing the spiral arms.

In the BM velocity residual map we see how the velocities at the maximum gas concentrations in the outer spiral arms are directed outwards. Outside these arms the residual velocities are directed inwards. This is in agreement with the expected gas flow outside CR, where the gas streaming relative the spiral pattern is counter-clockwise in Fig. 17a and moves inwards towards the outer arm. The gas hits the arm from the outside and thereafter streams along the arm in an outgoing motion. This behaviour is also illustrated by the streamlines in Fig. 16a. In the inner spiral arm, lying inside CR, the velocity pattern is the opposite. Gas, now streaming clockwise in Figs. 16 and 17, hits the arm from the inside in an outgoing motion and then follows the arm moving inwards. This arm will be further discussed in Sect. 6.1.2.

A very similar velocity pattern relative to the spiral arms can be seen in the observed H I map in Fig. 17b, where the situation is more clear on the SE side. The velocities are outgoing in the SE outer H I arm, and outside this arm the velocities are ingoing. The velocities change from outgoing inside the SE inner arm to ingoing outside this arm. The change takes place at the maximum H I density which coincides with the dust lane along the corresponding optical spiral arm.

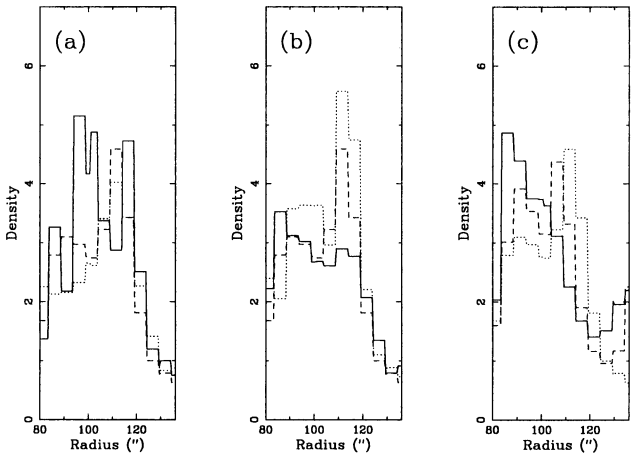

Fig. 18a–c. Gas surface density profiles, along the bar major axis, for nine different models, where the x-axis shows the distance from the centre **a** for pattern speeds 18 (solid), 19 (dashed) and 20 km s^{-1}kpc^{-1} (dotted), **b** for bar potential amplitudes 0.8 (solid), 1.0 (dashed) and 1.2 (dotted), **c** for physical relative bar lengths of 0.85 (solid), 0.92 (dashed) and 1.00 (dotted)

In the region between the two H I arms the situation is not as clear. This is the region of CR in BM, and the velocity field is not very well fitted here. Observations indicate inward motion between the arms, while BM has circular, or outward motion. The region around CR can be difficult to model since the gas is very sensitive to details in the forces due to large orbital periods in the reference frame of the bar.

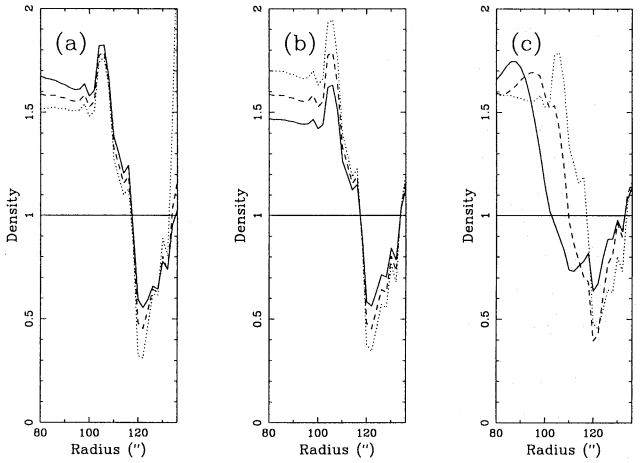

Fig. 19a–c. Relative gas surface density response along bar major axis computed in the linear approximation, using the same input parameters as for the models in Fig. 18, but using just the dominant $\cos 2\theta$ term of the perturber. The x-axis shows the distance from the centre **a** for pattern speeds 18 (solid), 19 (dashed) and 20 km s^{-1}kpc^{-1} (dotted), **b** for bar potential amplitudes 0.8 (solid), 1.0 (dashed) and 1.2 (dotted), **c** for physical relative bar lengths of 0.85 (solid), 0.92 (dashed) and 1.00 (dotted). This plot is thus the theoretical counterpart to Fig. 18 in the linear approximation

In the bar region we see evidence of strongly elliptical motion as will be discussed further in Sect. 6.1.3.

6.1.2. Inner arms at the end of the bar

The model BM has inner trailing arms emanating from the ends of the bar at $R \sim 110''$. The radial position, along the bar major axis, for this arm feature does not depend noticeably on the pattern speed and bar potential amplitude, but is sensitive to the adopted physical length of the bar. Increasing the bar length pushes the position of the arm outwards in the galaxy.

This behaviour is illustrated in Fig. 18 where we show traces of the gas surface density, along the bar major axis from the centre outwards, for nine different models. The first three models have fixed $A_{\rm bar} = 1.0$ and pattern speeds of $\Omega_{\rm p} = 18, 19$ and 20 km s^{-1}kpc^{-1} respectively (**a**), the next three models have fixed $\Omega_{\rm p} = 19$ km s^{-1}kpc^{-1}, and bar potential amplitudes of $A_{\rm bar} = 0.8, 1.0$ and 1.2 respectively (**b**), and the last three models have different physical lengths of the bar (**c**). The relative bar lengths in this last case are 0.85, 0.92 and 1.00, the pattern speed is 19 km s^{-1}kpc^{-1} and the bar potential amplitude is 1.0.

For seven out of nine models we encounter a density increase when entering the inner arm at $R \sim 110''$, while, outside this arm feature, the density decreases rapidly and thus defines the arm outer edge at $R \sim 120''$ in the direction of the bar major axis. For the two remaining models (Fig. 18c), having shorter bars, the density peak and the arm edge position are moved inwards. We also see in Fig. 18b a correlation between the arm amplitude and the bar potential amplitude $A_{\rm bar}$. A stronger bar results in a higher inner arm density contrast.

In order to investigate this behaviour in more detail we compute the corresponding gaseous responses in the linear epicyclic approximation.

We introduce the coordinate system ξ, η, where ξ and η are deviations from circular motion due to the non-axisymmetric part of the potential $\Phi(R, \theta)$ in Eq. (3). ξ is the deviation in the radial direction from the radius R, and η is the deviation along the circular arc with radius R.

The expressions, in the linear epicyclic approximation, for $\xi(R, \theta)$ and $\eta(R, \theta)$ have been given by Sellwood and Wilkinson (1993, Eq. (10)). Using, for clarity, just the dominant component $\Phi_2 \cos(2\theta)$ of the perturber, the expressions may be written

$$\xi(R, \theta) = \frac{\omega C + 2\Omega D}{\omega(\kappa^2 - \omega^2)} \cos 2\theta \tag{6}$$

$$\eta(R, \theta) = [-\frac{2\Omega(\omega C + 2\Omega D)}{\omega^2(\kappa^2 - \omega^2)} + \frac{D}{\omega^2}] \sin 2\theta \tag{7}$$

where $C(R) = -d\Phi_2/dR$, $D(R) = -2\Phi_2/R$, and $\omega = 2(\Omega - \Omega_{\rm p})$ is the angular frequency with which a particle in circular orbit overtakes the perturbation.

The solution (6,7) is valid away from resonances and describes the closed path of the guiding centre of the orbit in the limit of zero damping. The additional epicyclic motion around the guiding centre, contained in the full solution, is damped out if some damping term is present, and is not included in our hydrodynamic considerations (LL94).

The perturbed surface density, σ, over the unperturbed state, σ_0, may be derived from the continuity equation. For small displacements we can combine Eqs. (1E-4) and (1B-45) of Binney & Tremaine (1987) to get

$$\frac{\sigma}{\sigma_0} \sim 1 - \frac{\xi}{R} - \frac{1}{R}\frac{\partial \eta}{\partial \theta} - \frac{\partial \xi}{\partial R} - \frac{\xi}{\sigma_0}\frac{d\sigma_0}{dR} \tag{8}$$

The first three terms on the right hand side of Eq. (8) arise from the variation of the density along the orbit, the fourth from the crowding of orbits, and the fifth is due to the displacement of the surface density distribution. Assuming that the unperturbed surface density has a flat distribution cancels the last term.

Using this linear approximation approach we calculate the value of σ/σ_0, along the bar major axis, using the same input parameters as for the models in Fig. 18, but just using the $\Phi_2(R) \cos 2\theta$ term of the perturber. The result is presented in Fig. 19, where we see that the behaviour of σ/σ_0 near the position of the inner arm is very similar to the behaviour seen in the non-linear computations.

By looking more carefully at the different terms on the right hand side of Eq. (8), we find that the term dominating the shape of σ/σ_0 at the arm position is $\partial\xi/\partial R$. Thus orbit crowding and orbit rarefaction seem to be the causes of the arms emanating from the ends of the bar.

The question now is which terms in $\partial\xi/\partial R$ are dominating. By working out this derivative analytically and comparing the different terms, we find that the force derivative term containing $d^2\Phi_2(R)/dR^2$ and the force term containing $d\Phi_2/dR$ dominate $\partial\xi/\partial R$. These gradients are large around the end of the bar.

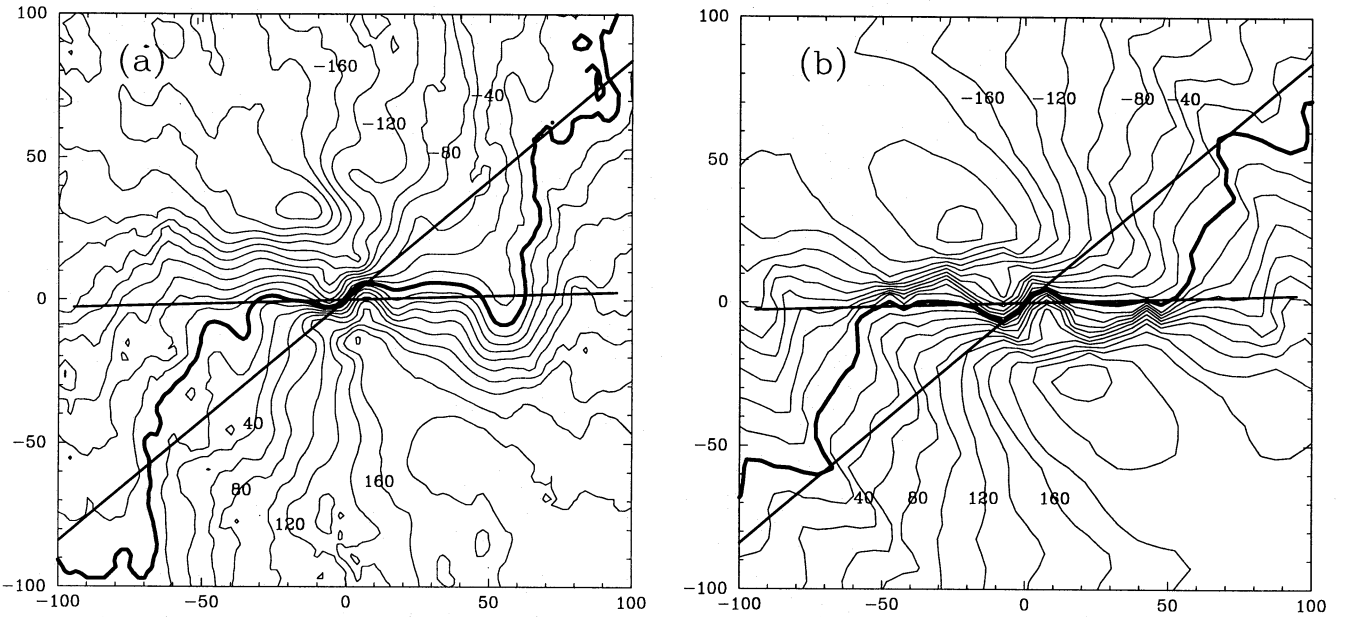

Fig. 20a and b. The optical radial velocity field in the inner $R < 100''$ of NGC 1365 (**a**), and the corresponding BM velocity field (**b**). The bar major axis (PA=92°) and the galaxy minor axis (PA=130°)are marked by the straight lines. The thick contour corresponds to the zero velocity, and the contour interval is 20 km s^{-1}

These deliberations together with the results from the simulation experiments lead us to conclude that the origin of the arm is due to the ending of the bar.

If no damping is present in the epicyclic approximation, the strength of the inner arm is a rapidly decreasing function of phase angle, and no distinction can be made between trailing and leading arms. However, if damping terms are included in the linear equations (LL94), the inner arm strength is kept for a longer phase interval.

The inner H I arms basically show a ring or square structure approximately at the radius of model CR. This structure is reproduced to a large extent by BM. However, there is H I gas tracing the inner bright optical arms across CR in contradiction to the inner arms in model BM, where the arms tend to become parallel to the CR circle as it approaches CR. Just inside CR the model arm contrast vanishes. Thus, in our bar + disc models the observed behaviour cannot be reproduced.

In order to drive a gaseous arm across CR we adopt a perturbing potential having both a bar and a spiral component. The results of this approach is discussed in Sect. 6.2.

6.1.3. The bar region and offset gas lanes

The morphology in the bar region of NGC 1365 is dominated by the offset dust lanes situated on the leading side of the bar major axis and by the CO concentration in the central region.

The observed dust lanes in NGC 1365 are fairly well matched by the corresponding gas lanes of model BM, as can be seen in Fig. 15a and bb. The model gas lanes require an ILR to be present, in good agreement with the results of Athanassoula (1992). Fig. 21 compares the model gas distribution with the observed CO distribution. Fat contours correspond to the density distribution in model BM, while thin contours are the $J = 2 - 1$ integrated line emission from Sandqvist et al. (1995). The model density has been smoothed to the resolution of the CO observations, i.e. $\sim 20''$. The CO observations reveal at least two components; an elliptical component centred on the nucleus, and a component extended along the dust lanes, which is very similar to what is seen in model BM.

The most obvious region of observed non-circular streaming in Fig. 17b is the bar region, where strong velocity residuals are present. Similar residuals are seen in the corresponding map for BM (Fig. 17a) due to strongly elliptical motion. At the positions of the gas lanes in BM, the model velocities in the radial direction change sign from outward going to inward going motion. For elliptical orbits, oriented strictly parallel to the bar major axis, the change of sign would occur at the bar major axis. In the damped case, however, illustrated in Fig. 12, the rapid change of motion is shifted to the leading side of the bar. This behaviour is mainly due to the effect on the orbits caused by the ILR.

The observed and BM radial velocity fields for $R < 100''$ are shown in Fig. 20a and b. Outside $R \sim 10''$, the observed contours are consistent with motion along twisted elliptical orbits, inclined with respect to the bar major axis, as found in BM. The observed zero contour follows the bar major axis out to $\sim 50''$, again consistent with the streaming in BM. Outside $R \sim 50''$ the BM model orbits become increasingly more circular when approaching the projected bar end at $\sim 90''$, which is reflected by the zero velocity contour approaching the minor axis of the galaxy. This trend is clearly seen in the observed velocity field.

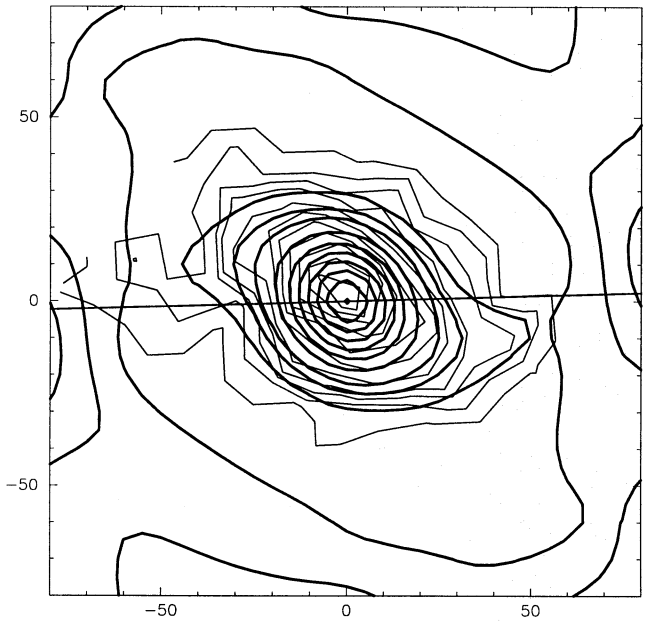

Fig. 21. The density distribution from model BM, smoothed to $\sim 20''$ resolution (thick) overlaid on the CO $J = 2-1$ integrated line emission from Sandqvist et al. (1995) (thin). The relative contour levels are the same for both distributions

Table 1. Offset coordinates for reference points

Ref. point	$x = -\Delta\alpha \cos\delta$ ($''$)	$y = \Delta\delta$ ($''$)
nucleus	0	0
H II reg. L2	4.59	−5.42
H II reg. L4	−16.56	16.39
H II reg. L32	−37.58	24.00
H II reg. L33	−29.07	19.40
star D	62.63	13.25
star E	33.10	71.21
star F	−53.15	−147.16

In Fig. 22 we present the slit observations, covering the bar region, together with the BM model radial velocities at the same positions. We only present slits showing relevant deviations from pure circular motion. The observed velocities are plotted as open circles, and the model velocities by the solid curves. The pure rotational motion, from the rotation curve in Fig. 4, is represented by the dotted line. The slit positions are shown in Fig. 23. In Fig. 24 we have plotted the Hα and [N II] velocities from the very central region of one of our slit observations (slit no. 1 in Fig. 22) where the slit crosses the nucleus having a position angle of 138°, close to the position angle 130° for the minor axis. Moving along the slit in the direction of the position angle, i.e. away from the observer, the radial velocities are first negative, become zero at $\sim -5''$ and then positive until crossing the nuclear position. On the opposite side of the nucleus the velocities are negative out to $\sim 5''$ where they become positive again. Considering that the position angle of the slit is larger than that of the minor axis and that the NW side is the near side, this behaviour is consistent with elongated orbits perpendicular to the bar in the nuclear region inside $\sim 5''$ and may be taken as evidence for the existence of orbits of the x_2 family.

The flow pattern in the model BM is illustrated in Fig. 16. In the bar region the flow follows twisting elongated orbits consistent with the model having an ILR at $\sim 27''$. The direction of the flow is changed when crossing features like the spiral arms and offset gas lanes, indicating the presence of shocks. Inside the inner arms, located inside CR, the flow is on elongated orbits. When hitting the inner arms, the flow is redirected towards the bar major axis due to the loss of angular momentum in the shock.

Taking into account the complicated details of the structure of the observed galaxy and its asymmetry, the agreement between the observations and BM can be considered satisfactory, particularly since the general streaming motions in NGC 1365 seems to be well described by BM.

Since model features do not exactly overlap their observed counterpart, direct detailed comparisons between observed slit and model velocities can be misleading. Nevertheless we have chosen two slits that probe interesting regions for a more detailed comparison.

1. *No.11 in Fig. 22.* This slit has a position angle of 90° and is centred on the H II region L2. The slit passes 5.″4 south of the nucleus and crosses the apparent minor axis $\sim 10''$ eastward from the reference point in the slit direction (see Fig. 23). Had the motion been purely circular, the radial velocity at the position of the minor axis would be equal to zero and would have a steep gradient, as shown by the dotted line.
   In the region close to the reference point the line-of-sight velocity component is nearly equal to that of circular motion. Close to the minor axis the velocity turns sharply upwards again and remains positive out to $\sim 50''$ while decreasing to lower values. This observed trend is very well reproduced by BM, where elliptical orbits in this region keep a positive radial velocity component for a longer interval than would be the case for pure circular motion (see Figs. 16 and 20a and bb).
2. *No.12 in Fig. 22.* We choose this spectrum because it crosses a dust lane both in the model and in NGC 1365. The reference point is the H II region L33 located in the NE dust lane along the leading side of the bar. The slit lies almost perpendicular to the dust lane. It crosses the apparent minor axis at $\sim -42''$, and the potential minimum of the bar at $\sim -19''$ from the reference point along the slit. Over this range the observations show positive radial velocities of the order of +60 kms^{-1}, indicating strongly outgoing motions in the bar. There is also a sharp gradient at the position of the H II region.
   A very similar behaviour is observed in BM, where the sharp gradient at the position of the gas lane is explained by the shock due to the effect of the ILR. In both BM and

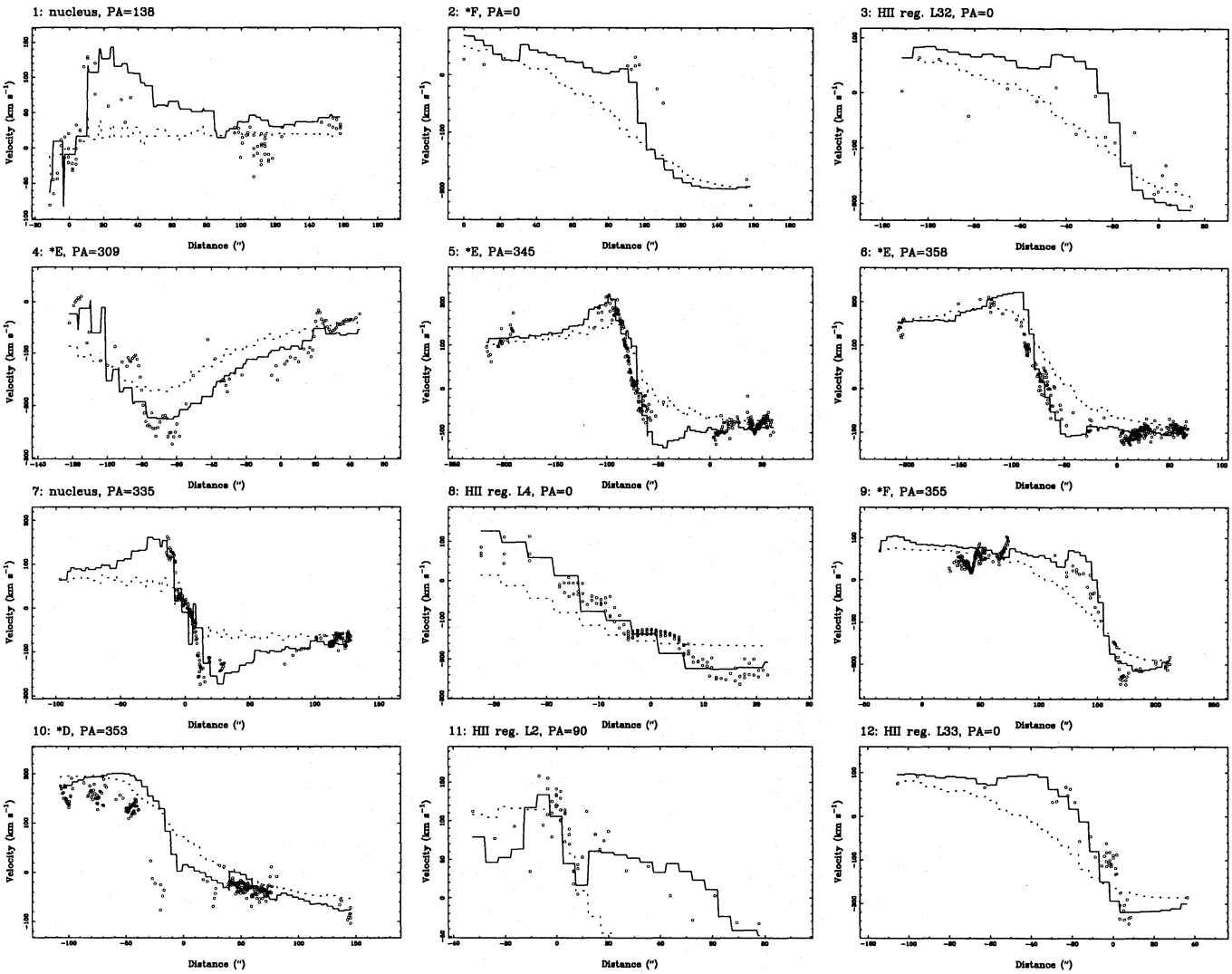

Fig. 22. Observed velocity slits that show relevant deviations from pure circular motion. The observed velocities are plotted as open circles, the BM velocities are represented by the solid curve, and the dotted line corresponds to pure rotational motion according to the rotation curve in Fig. 4. The number of each spectrum is given in the upper left corner of each panel together with an identification, containing information on the reference point and the position angle of the slit. The positions of the reference points are given in Table 1. The x-axis gives the distance along the slit, in arcsec, increasing in the direction of the position angle, and equal to zero at the position of the reference point. The positions of the slits are shown in Fig. 23

NGC 1365 the zero radial velocity is crossed to the north of what would be expected from pure circular motion. As shown by Jörsäter (1984) the stellar velocities along this slit do not show the steep velocity gradient of the interstellar gas.

6.2. A bar + disc + spiral model; BSM

The J-band image shows that the bright star forming optical arms are superposed on stellar density enhancements. This is in agreement with the conclusions of Elmegreen & Elmegreen (1985) from their sample of 16 barred galaxies. In order to investigate the effects of an additional spiral perturbing potential we extract a representative spiral potential from the J-band image (see Sect. 4.2.4), and compute a new set of models containing both a bar and a spiral potential.

The problem here is that the parameters are cross-correlated to a larger extent than for the bar + disc models. For the bar + disc models the position of the outer arm is almost totally controlled by the pattern speed, although a small effect towards tighter arms when using stronger bars was found. In the case of a bar + spiral perturbing potential we found that increasing the spiral potential results in a decrease of the radial extent of the outer arms, which is also the effect seen when increasing the pattern speed. This means that we can get similar results from our calculations for a range of different pattern speeds and bar + spiral perturbing potential amplitudes. From a number of computations the range of possible values giving acceptable

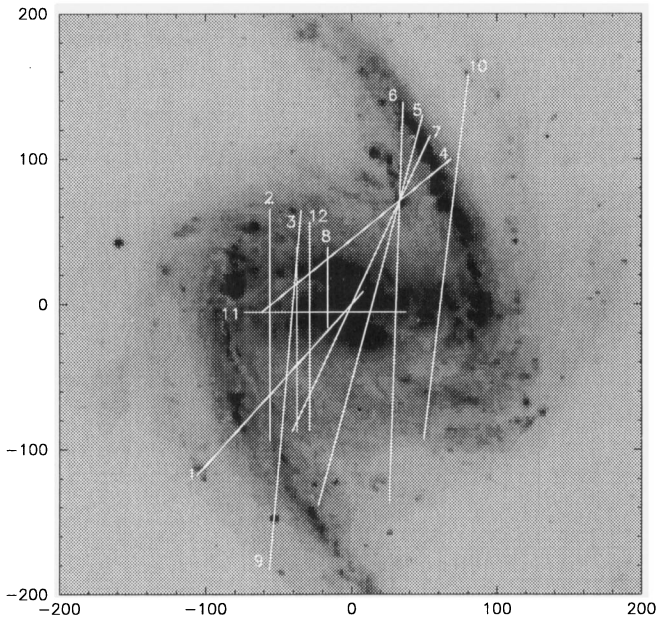

Fig. 23. Optical slit positions overlaid on a gray scale map of NGC 1365. The numbers corresponds to the numbers in the labels of Fig. 22

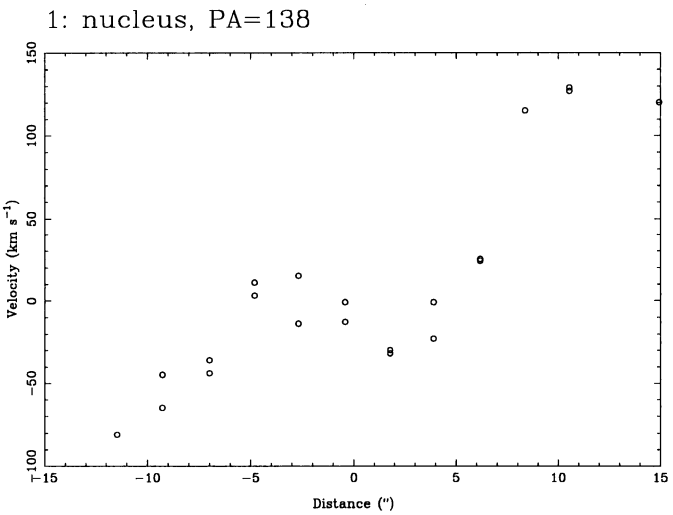

Fig. 24. Observed radial velocities along slit no. 1 in Fig. 22 crossing the nucleus in a position angle of 138°. The scale on the x-axis is arcseconds offset from the nucleus in the direction of the position angle

fits to observations was estimated to be: $17 < \Omega_p < 19$ km s^{-1}kpc^{-1}, $0.8 < A_{bar} < 1.4$ and $0.2 < A_{spiral} < 0.6$. We will present here only one of the possible models that resemble the observations, hereafter referred to as BSM. The main parameter values for BSM are: $\Omega_p = 18$ km s^{-1}kpc^{-1}, $A_{bar} = 1.2$ and $A_{spiral} = 0.3$. The rotation curve is the same as for model BM.

A value of $A_{spiral} = 0.3$ means that the M/L_J ratio for the spiral luminosity is 30% of the M/L_J ratio for the bar, and the pattern speed $\Omega_p = 18$ km s^{-1}kpc^{-1} gives the main resonance radii at $R_{ILR} = 30''$, $R_{CR} = 157'' = 1.31R_{bar}$ and $R_{OLR} = 232''$.

The gas response of BSM is presented in Fig. 25 as a contour plot, overlaid on the gray scale H I total column density map, and overlaid on the optical B image.

The problem of driving the inner spiral arm across CR, encountered in models with just a pure bar perturbation is reduced when including the spiral component. We see that in BSM the inner arm follows the observed optical arm out to approximately $R = 190''$, thus across model CR at $R = 157''$, and then turns towards being parallel to the outer main arm. This turning of the model arm is not consistent with observations, where the optical bright arm joins the main H I arm at $R \sim 250''$. The reason for this discrepancy could be that our surface density Fourier components are truncated at $R \sim 200''$, which is the limit of our J-band image.

The overlapping of the outer model arms with the main H I arm is better in BSM than in BM, and the similarity of the model velocity field and the observed velocity field (see Fig. 27) is also improved, particularly in the region between the inner and outer spiral arms.

The BSM velocities at the observed slit positions are essentially the same as for BM, since the regions that the slits cover are mostly at small radii and thus not strongly affected by the added spiral perturbation. The central gas distribution in BSM is very similar to the one in BM, and the comparison with the CO distribution gives very much the same result.

In Fig. 26 we present the flow pattern from BSM, corresponding to Fig. 16 for BM. In BSM the gas experiences a strong redirection, i.e. shock, all the way up to CR. At CR the gas flows around the Lagrangian points and is redirected, at the position of the massive spiral arm, along the spiral arm. Outside CR, collision occurs between the gas flowing around the Lagrangian points and gas streaming in normal rotational motion. The collision front outlines the continuation of the inner arm outside CR.

6.3. Model using a modified rotation curve; BSM2

There is one region where the fit of models BM and BSM to the H I density is not satisfactory and that is the outermost part, i.e. at radii larger than $R \sim 240''$. This could have been expected since both part of our data and our numerical code are not adequate for that region. Our code is planar and two-dimensional, while NGC 1365 seems to have a sizeable warp in its outer parts (JvM), which also affects the derivation of the rotation curve. Furthermore the J-band image from which we extracted our perturbing potential extends only to $R \sim 200''$, and values of the perturbing density at larger radii can only be obtained by extrapolation, an obviously unsafe procedure. Nevertheless it is still interesting to check what effect a small change in the rotation curve could have on the model. We thus ran some models with a somewhat less abrupt fall of the rotation curve thereby lowering the effect of the warp. Fig. 28 shows the density response for a model fairly similar to BSM, hereafter BSM2, overlaid on the H I density gray scale plot. The rotation curve has been raised by less than 10 km s^{-1} (i.e. within the observational uncertainties) in the region between $220'' < R < 340''$, the adopted

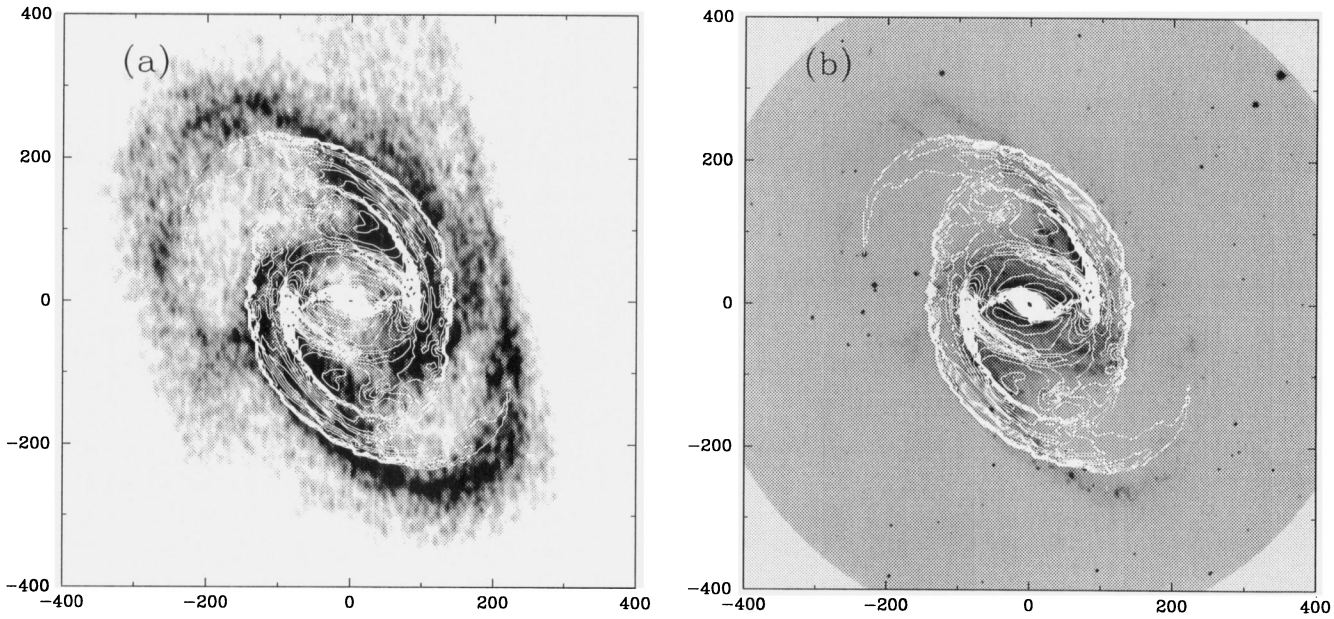

Fig. 25a and b. The BSM density contour map overlaid on the total column H I density map (**a**) and on the optical map (**b**)

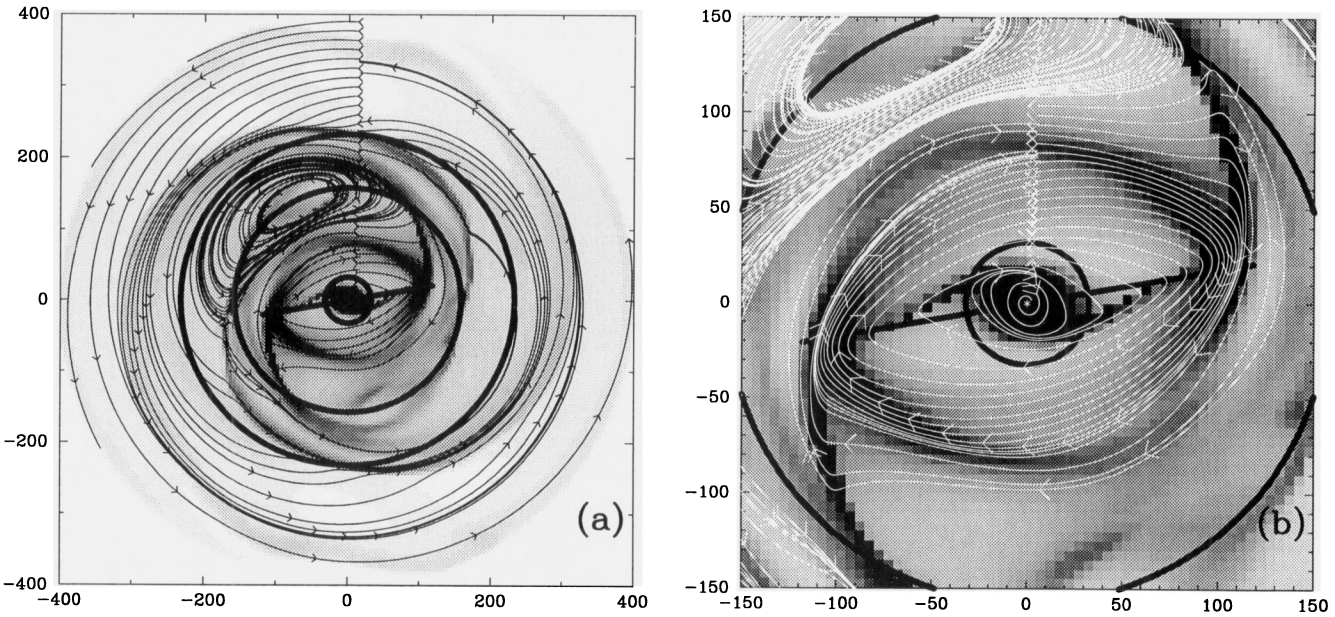

Fig. 26a and b. Gas flow lines from BSM overlaid on density gray scale maps of BSM. **a** Full scale, **b** bar region. The model is seen face-on and the bar major axis is indicated by a straight line. The circles mark the ILR, CR and OLR resonance positions

pattern speed is $\Omega_p = 17$ km s^{-1}kpc^{-1} and the spiral amplitude $A_{spiral} = 0.4$. One can see a very substantial improvement of the fit of the outer southern arm in the outer parts, proving that such a fit is indeed possible. It is thus possible to obtain a satisfactory fit of the outer arm using only the bar and spiral forcing rotating at the same pattern speed.

6.4. Self-gravitating models; BMSG, BSMSG

In this section we consider the effects of self-gravity, which could be non-negligible as the gas to stellar mass ratio for NGC 1365 is ~ 0.1 (e.g. Wada & Habe 1992, Friedli & Benz 1993). Since the evolution of the gaseous and/or stellar system to its present form is beyond the scope of this paper we only test the effects of self-gravity on the final quasi-stationary states of the BM and BSM models.

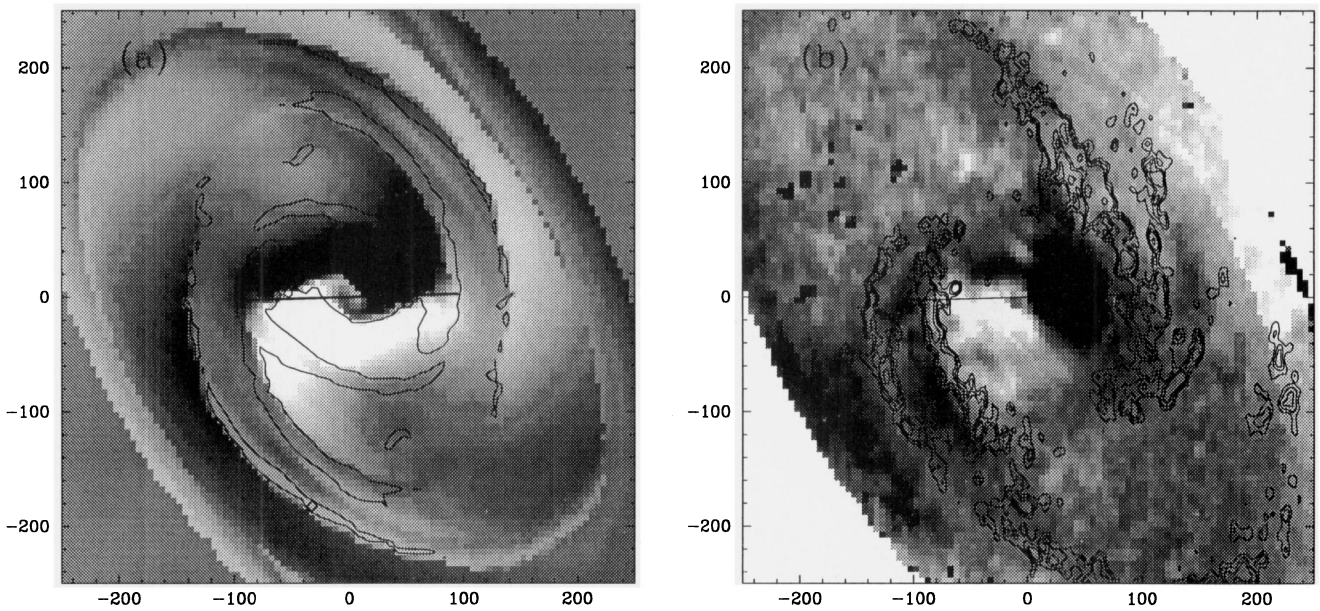

Fig. 27a and b. Velocity residual maps, after subtraction of the rotation curve from Fig. 4, with density contour overlays: **a** for the model BSM, **b** for H I data

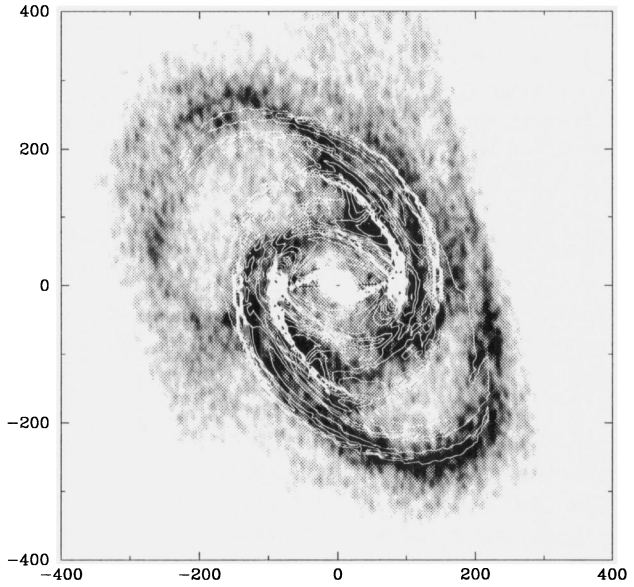

Fig. 28. The BSM2 density contour map overlaid on the total column H I density map. The straight line through the centre marks the position and length of the model bar major axis

Since in the previous simulations the gas contribution is included in the axisymmetric forces but not in the non-axisymmetric perturbations, we have to include self-gravity as follows: Let us refer to the forces from the model input rotation curve by $\mathbf{F}_{\rm ROT}$ and the perturbing, non-axisymmetric, forces from the stellar component by $\mathbf{F}_{\rm SPER}$. Averaging the BM (respectively BSM) final gas density distribution azimuthally and scaling the total gas mass to be 10% of the stellar mass in the galaxy, measured out to $\sim 400''$, we calculated the corresponding forces, which we will refer to as $\mathbf{F}_{\rm GROT}$. At every step of the simulation we scaled the gas distribution correspondingly, and calculated the total gas forces $\mathbf{F}_{\rm G}$, using the gas densities on the simulation grid and FFTs. The forces, $\mathbf{F}$, acting in the self-gravitating models are then computed as:

$$\mathbf{F} = \mathbf{F}_{\rm ROT} - q\mathbf{F}_{\rm GROT} + q\mathbf{F}_{\rm G} + \mathbf{F}_{\rm SPER} \qquad (9)$$

where q is a factor growing linearly from 0 to 1 in 0.1 Gyr, in order to introduce gradually the non-axisymmetric forces due to the gas. To avoid numerical problems due to sharp density gradients in the models, we convolve the gas density distribution with a Gaussian, having a FWHM of $10''$, before each computation of the forces $\mathbf{F}_{\rm G}$. The chosen width is similar to the width of the H I arms. The self-gravitating models are evolved for one additional Gyr after the nonaxisymmetric forces have reached their maximum amplitude, starting with the quasi-steady state of BM or BSM.

In Fig. 29 we present the response from BM (**a**), and BSM (**b**) together with the response from the corresponding self-gravitating models BMSG (**c**) and BSMSG (**d**). Both BM and BSM have here been evolved for 2 Gyrs in order to be comparable with the self-gravitating models. The general effect of self-gravity on the models is to decrease somewhat the radial extent of the outer spiral features. Model BMSG shows a complex evolving structure in the CR region, which leads us to conclude that model BM is not as stable in time as BSMSG, which remains basically unaltered.

During the model evolution, both with and without self-gravity, there is a strong inflow of gas crossing the ILR radius

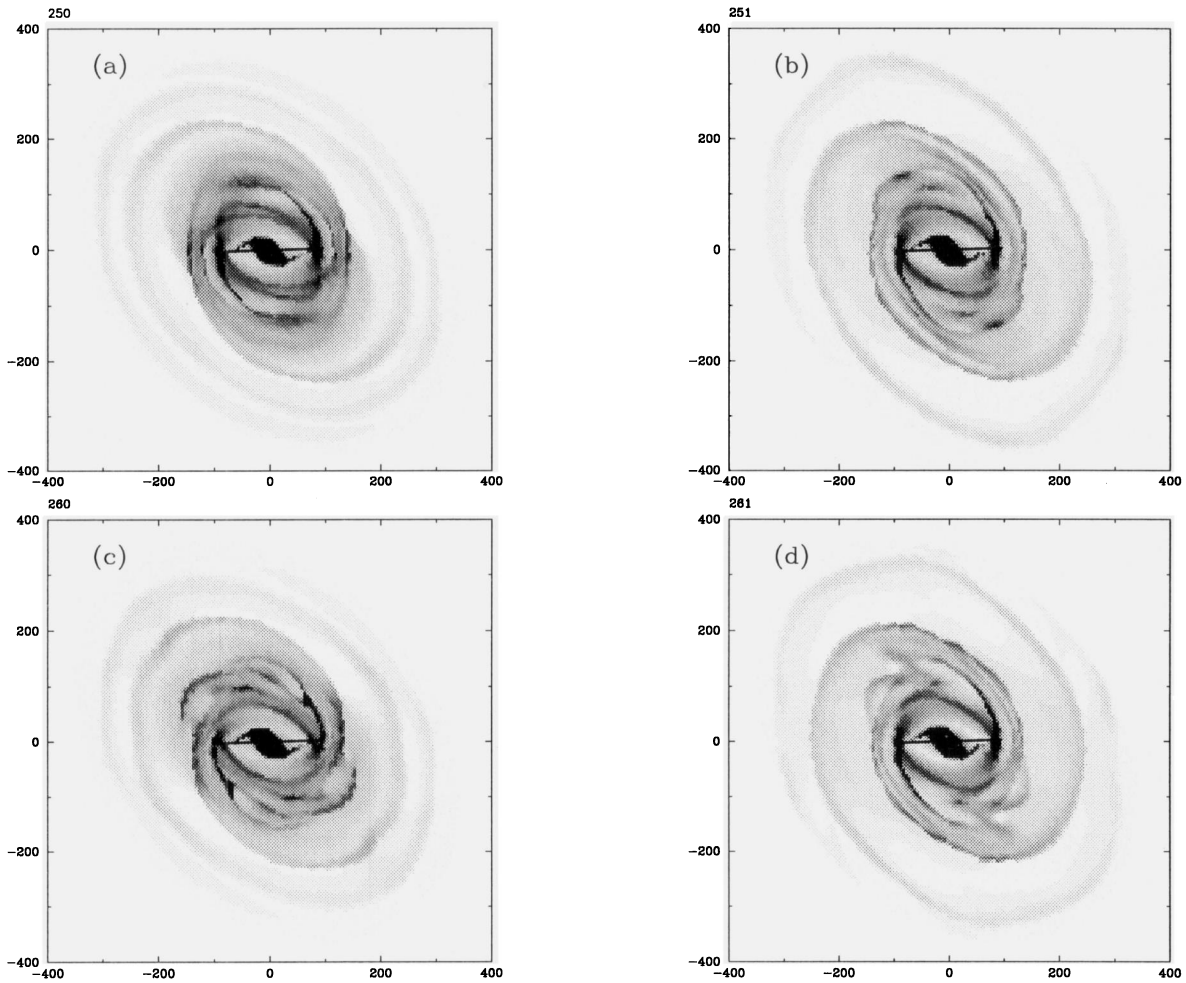

Fig. 29a–d. Gray scale density response from BM (**a**), from BSM (**b**), together with the response from the corresponding self-gravitating models BMSG (**c**) and BSMSG (**d**)

$R \sim 27''$, which builds up a central mass concentration. During the self-gravitating phase of model BSMSG there is a steady inflow of gas into the inner $R < 27''$ of $\sim 2M_\odot$/yr. The corresponding number for BMSG is $\sim 1M_\odot$/yr. Thus the presence of a spiral potential increases the inflow rate towards the nucleus. The difference in mass transfer between the nonself-gravitating models and the self-gravitating models is marginal.

It is interesting to ask whether this inflow rate could eventually lead to the destruction of the bar (e.g. Hasan & Norman 1990, Friedli & Benz 1993, Friedli 1994). According to Friedli (1994) the bar would dissolve for a central mass of 2% of the total stellar disc mass. Lets assume that all *stellar* mass ($3.55 \times 10^{11} M_\odot$) is located in the disc and, furthermore, that the central mass initially is equal to zero and grows just by accumulating gas at a steady rate of $2M_\odot$/yr. This gives us an upper limit on the life-time for the bar of $T_{\rm bar}$ = 3.55 Gyrs, i.e. roughly 10 bar rotations. Assuming that half the stellar mass is in the disc, which seems more reasonable, we find 5 bar rotations, i.e. a very low estimate for the life time of the bar. It should be noted, however, that if star formation is included, there should be less gas available and therefore less inflow and the life time of the bar will be longer (Friedli & Benz 1995).

6.5. Star formation

In order to trace the regions of "star formation" in our models we included a simple gas-star interaction recipe (cf. Athanassoula 1992), which removes gas from high density regions, thus very crudely mimicking star formation, and adds gas uniformly over the grid, thus mimicking mass loss from stars. This was activated after the models BM and BSM had reached a quasi-steady state, and the models were then evolved for one additional Gyr. The central gas concentration quickly decreases, but the model offset gas lanes remains. The resulting "star formation" maps do not strictly trace star formation, but rather show regions where high compression of the gas has occurred, i.e. regions favourable to star formation. Both models show such high compression regions in the offset gas lanes along the bar, at the end of the bar and in the inner spiral arms. The "star formation" in the outer arm is low for both models, which would explain the difference in appearance of the optical and H I outer arms.

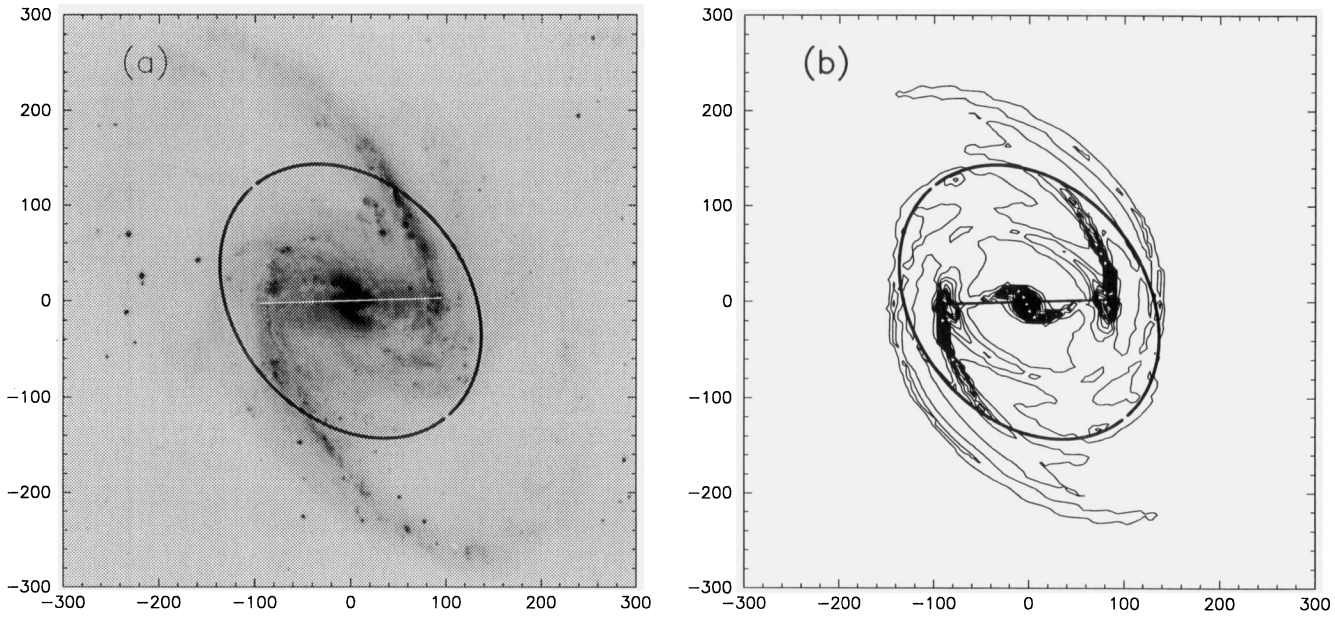

Fig. 30a and b. The optical blue image of NGC 1365 (**a**), together with regions with strong star formation in BSM (**b**). The straight line marks the position of the bar major axis, and the ellipse represents the CR radius for the model BSM

Furthermore, it is more extended at the inner arm for BSM than for BM, as expected, since the gas in the former model experiences a stronger shock when entering the potential minimum in the arm. Of course high gas density is not the only ingredient necessary for star formation. Thus, Athanassoula (1992, 1994) showed that no star formation should be expected in the straight gas lanes along the bar because of the high shear present there. Taking this into account, we find that there is a very good agreement between the results of our models and observations, with a strong tendency to form stars in the inner arm and at the end of the bar and almost no star formation in the outer optical arms (see Fig. 30). The match is even better if we compare with a continuum-subtracted Hα image (obtained by S. Jörsäter, unpublished), which indeed describes star formation better. The "star formation maps" show a rapid decrease in star formation outside CR, in agreement with observations. This is explained in the models by the fact that shocks are less violent outside CR, where the streaming is almost circular.

7. Conclusions

We have performed hydrodynamical modeling of the barred spiral galaxy NGC 1365, using observations as far as possible to restrict the values of the free parameters.

We show that the density and velocity structure of a barred spiral galaxy may be reproduced on most scales with a rather simple model. The bar potential shape, and the rotation curve outside $R > 120''$, have values directly from observations. In the inner region $R < 120''$ we use a rotation curve that is consistent with the observed optical slit velocities to the first order, when the perturbations of the bar have been taken into account. The pattern speed has a value in BM and BSM that puts CR at a radius $R_{\rm CR} \sim 145'' = 1.21 R_{\rm bar}$ for BM and $R_{\rm CR} \sim 157'' = 1.31 R_{\rm bar}$ for BSM, where $R_{\rm bar} = 120''$ is the optical semi major axis of the bar. This is in agreement with the value $R_{\rm CR} = (1.2 \pm 0.2) R_{\rm bar}$ found by Athanassoula (1992). The spiral potential in the models has the same spatial location and spatial shape as that of the observed bright optical arms in the J-band image, although the actual amplitude is a free parameter. The main conclusions from this work are:

7.1. Morphology and velocity field

Our models reproduce the main features of the general morphology and velocity field in NGC 1365. We found no need for any unobserved potential components in order to drive the outer observed H I spiral features. In our models, where the gas is not self-gravitating, the spiral arms naturally have the same pattern speed as the bar. The agreement between the models and observations gives no motivation for assuming different pattern speeds.

The SE spiral feature of our best models coincides nicely with the observed outer SE main H I spiral arm. The NW H I arm is somewhat more complex, but even there a reasonable fit is achieved. Outside $R > 240''$ the model spiral arm bends earlier than the observed H I arm, but this could partly be due to the uncertainty in the rotation curve caused by warp effects. A small change in the rotation curve can improve the fit in this region, as is demonstrated by model BSM2. The associated observed H I velocity residuals are reproduced, in the sense that *outside* the outer arm there is evidence for inward streaming motion in both the models and in NGC 1365, and *in* the arm there is outward motion in both the models and NGC 1365. In the region

between the outer and inner H I arms the fit is better for BSM than for BM.

The inner H I arms, coinciding with the inner parts of the bright optical arms in NGC 1365, are reproduced in the models, where the model arms are driven by the non-axisymmetric forces and force derivatives due to the ending of the bar, i.e. a decrease in the bar surface density. Thus, there is a natural coupling between the end of the bar and the inner spiral features. The model velocity residuals show outward going motion *inside* the inner arms and inward going motion *in*, and just *outside*, the arms, qualitatively consistent with observations. The bar + disc model BM is not able to drive these inner arms across the model CR at $R \sim 145''$, in contrast to observations where the inner optical arms extends all the way out to the main H I arms. We can overcome this problem by including a spiral potential in our bar models. The spiral potential accelerates gas circling around the Langrangian points inside the spiral potential *outwards*, and the gas outside the spiral potential *inwards*, thus creating a collisional front at the position of the arm. This collisional front outlines the continuation of the arm outside CR.

In model BSM, having CR at $R \sim 157''$, the inner model arms overlap the observed optical arms out to $R \sim 190''$. Outside, the model arms bend off earlier than the observed arms, which could be due to the truncation of the observed J-band Fourier components at $R = 200''$, which is the limit of the J-band image. The streaming in and around the outer as well as the inner arms, displayed in both the models and the observations, agree with what is expected of density wave behaviour in a gas.

The observed morphology and velocity field in the bar region is well reproduced by our models. The model offset gas lanes have approximately the same spatial positions and extent as the observed dust lanes. The CO observations, showing a strong central concentration and a weak tendency to be aligned with the dust lanes, are also reproduced by the models. Strong velocity gradients across the dust lanes are seen in both NGC 1365 and the models. The general motion in the bar region of NGC 1365, as measured by 28 optical long slits and H I velocity data, is consistent with the model streaming.

We favour the bar + disc + spiral model BSM, since both the morphology and velocity field are better fitted with this model. Furthermore, this model was naturally more stable in time, compared to BM, when self-gravity was included. The better fit with BSM compared to BM suggests the presence of massive spiral arms in NGC 1365.

7.2. Resonances

The radial extent of the dominating spiral arms in the model is a strong function of the pattern speed, i.e the positions of CR and OLR. The general principle in our bar + disc models, supported by linear gas orbit theory, is that orbits twist gradually over the OLR from being elongated perpendicular to the bar outside CR to parallel to the bar outside the OLR. This twisting causes orbit crowding, which then outlines the spiral features. For the bar + disc + spiral models the situation is more complex due to highly non-circular motion in the CR-OLR region, but still in rough agreement with the above principle.

Since the model outer arm nicely coincides with the observed H I main arm both for BM and BSM, we conclude that the gross morphology and velocity field in NGC 1365 is consistent with having a CR radius of $R_{\rm CR} \sim 150'' = 1.25 R_{\rm bar}$ and an OLR at $R_{\rm OLR} \sim 230''$. An even better fit in the outer region is obtained, as demonstrated with the model BSM2, if we modify the rotation curve, within the errors, so as to have an OLR at $R_{\rm OLR} \sim 245''$.

The existence of the offset gas lanes in the models requires an ILR to be present, and we have found this to be located approximately at $R_{\rm ILR} = 30''$. The orbits gradually twist over this ILR, from being perpendicular to the bar for $R < 5''$ to parallel to the bar outside the ILR, again consistent with periodic orbit orientation according to linear gas orbit theory and previous hydrodynamical simulations. The orbit crowding, due to this twisting, outlines the model offset gas lanes. Since the model gas lanes and the corresponding velocity field are consistent with the observed counterparts, we conclude that observations of NGC 1365 are consistent with having an ILR at $R_{\rm ILR} \sim 30''$.

We also find, in agreement with the results of Quillen et al. (1994) for the barred galaxy NGC 4314, that the bar in NGC 1365 terminates close to the 4 : 1 resonance of model BSM. This is also in agreement with the results of Contopoulos et al. (1989), based on stellar dynamical considerations.

7.3. Star formation

We find that the star forming regions in our models resemble well those in NGC 1365, with star formation predominantly in the inner spiral arms and at the end of the bar, which would explain the difference in appearance between the optical and H I outer arms. The strong star formation observed at the ends of the bar in NGC 1365 is reproduced in our models, and is due to collision between elliptical orbits inside the bar and more circular orbits just outside the bar. The model star formation regions are, to a large extent, confined inside the CR radius, which matches the observations well.

7.4. The effects of self-gravity

The introduction of self-gravity in the models creates a spiral potential that has the effect of decreasing the radial extent of the outer arms. In addition, model BMSG shows a complex evolving structure in the CR region, which leads us to conclude that model BM is not as stable in time as BSMSG, which remains basically unaltered. During the self-gravitating phase of model BSMSG there was a steady inflow of gas into the inner $R < 27''$ of $\sim 2 M_\odot$/yr, while the corresponding number for BMSG is $\sim 1 M_\odot$/yr, showing that the presence of a spiral potential increases the inflow rate towards the nucleus. This mass accretion could be responsible for the ILR present in NGC 1365, and could, ultimately, destroy the bar.

8. Final remarks

When modeling such a complicated system as a barred galaxy, one must be aware of the model limitations. Our aim was to see how much of the observed structure could be reproduced by this relatively simple model. A lot of CPU time-saving assumptions are included in the model. For example we assumed that the motions of the ISM can be modeled by a purely hydrodynamical scheme, we modeled the gas as an ideal isothermal gas, and assumed that the galaxy 3D-dynamics can be represented by 2D-calculations and by strict bisymmetry. Further, the grid size limits the resolution. Despite these simplifications, the general result of our modeling seems to be consistent with observations on most scales. Fine-tuning the models further does not seem to be warranted since the accumulated effects by the approximations probably have a greater influence on the models than small changes in the parameters.

Acknowledgements. We would like to thank Steven Jörsäter and Gustav van Moorsel for letting us use their H I data, G.D. van Albada for making available to us his version of the FS2 code and Alice Quillen and Jay Frogel for letting us use their J-band image of NGC 1365. We would also like to acknowledge the referee D. Friedli for many useful suggestions and comments, and Steven Jörsäter, Aage Sandqvist, A. Bosma, J. Sellwood and Pawel Artymowicz for stimulating discussions.

Appendix A: bar and spiral potential from Bessel functions

Since we observe only the surface brightness, i.e. the integrated brightness along the line of sight, we have no direct information about the brightness distribution along this line of sight. Observers claim a thickness of a bar somewhere between 7% and 25% of the bar major axis (e.g. Burstein 1979; Tsikoudi 1980). We have adopted the value 10% for the bar, i.e. 1 kpc, and, assuming the thickness to be less further out in the galaxy, 0.5 kpc for the spiral arms. We compute potentials from the surface brightness distribution assuming a constant M/L-ratio and a specific form for the distribution of matter with height above the $z = 0$ plane. We further assume that our non-axisymmetric density distribution $\rho(r, \theta, z)$ can be written as

$$\rho = F(z)\Sigma(r, \theta) \tag{A1}$$

where $F(z)$ describes the density distribution as a function of z and is normalized so that its integral over z is equal to unity. $\Sigma(r, \theta)$ is the observed surface density, assumed to be proportional to the observed surface brightness. We thus divide the observed surface density into density layers having different distances from the plane $z = 0$. The fraction of the total observed surface density in each layer is determined by the function $F(z)$, and the sum of these layers is, of course, equal to the total observed surface density $\Sigma(r, \theta)$.

To obtain the total potential in the plane of the galaxy we have to add up the contributions from the density layers at different distances from the galaxy plane.

$$\Phi(r, \theta) = \int_{-\infty}^{\infty} \Delta\Phi(r, \theta, z)\, dz \tag{A2}$$

where $\Delta\Phi(r, \theta, z)$ is the potential in the plane $z = 0$ from a layer at a distance z from this plane. This potential can be written as (see Binney & Tremaine 1987, Eq. (2P-8)).

$$\Delta\Phi(r, \theta, z) = \sum_{m=-\infty}^{\infty} \Delta\Phi_m(r, z) e^{\mathrm{i}m\theta} \tag{A3}$$

where

$$\Delta\Phi_m(r, z) = -G \int_0^{\infty} e^{-k|z|} J_m(kr) dk \int_0^{\infty} J_m(kR)\, R\, dR \int_0^{2\pi} \Sigma(R, \Theta)\, e^{-\mathrm{i}m\Theta}\, d\Theta \tag{A4}$$

where G is the gravitational constant and J_m is the cylindrical Bessel function of order m.

As our total surface density is described with the Fourier components

$$\Sigma(R, \Theta) = \sum_{m'} A_{m'}(R)\, e^{\mathrm{i}m'\Theta} \tag{A5}$$

we can move $\sum_{m'} A_{m'}(R)$ out from the last integral, and compute it directly

$$\int_0^{2\pi} \Sigma(R, \Theta)\, e^{-\mathrm{i}m\Theta}\, d\Theta = \sum_{m'} A_{m'}(R) \int_0^{2\pi} e^{\mathrm{i}(m'-m)\Theta}\, d\Theta = 2\pi\, \delta_{m,m'} \sum_{m'} A_{m'}(R) \tag{A6}$$

where

$$\delta_{m,m'} = \begin{cases} 1 & \text{for } m = m' \\ 0 & \text{otherwise} \end{cases} \tag{A7}$$

We can now, using the weighting function $F(z)$ in Eq. (A1) and the results in Eq. (A6), write Eq. (A4) as

$$\Delta\Phi_m(r, z) = -2\pi G \int_0^{\infty} F(z)\, e^{-k|z|} J_m(kr)\, dk \int_0^{\infty} J_m(kR)\, A_m(R)\, R\, dR \tag{A8}$$

For simple functions, $F(z)$, we can integrate Eq. (A8) over z analytically to obtain $\Phi_m(r)$, the mth azimuthal component of the potential in the plane of the galaxy.

We computed potentials for two different simple distributions. The first one is a top hat function

$$F(z) = \begin{cases} \frac{1}{2Z_0} & \text{for } |z| < Z_0 \\ 0 & \text{otherwise} \end{cases} \tag{A9}$$

which gives us the equation

$$\Phi_m(r) = -2\pi G \int_0^{\infty} \frac{1 - e^{-kZ_0}}{kZ_0} J_m(kr)\, dk \int_0^{\infty} J_m(kR)\, A_m(R)\, R\, dR \tag{A10}$$

The second one is a triangle function

$$F(z) = \begin{cases} \frac{1}{Z_0}(1 - \frac{|z|}{Z_0}) & \text{for } |z| < Z_0 \\ 0 & \text{otherwise} \end{cases} \quad \text{(A11)}$$

which gives us the equation

$$\Phi_m(r) = -2\pi G \int_0^\infty \frac{2}{k^2 Z_0^2}(kZ_0 + e^{-kZ_0} - 1)\, J_m(kr)\, dk \int_0^\infty J_m(kR)\, A_m(R)\, R\, dR \quad \text{(A12)}$$

Since our surface density is tabulated as discrete values, the integral over R in Eqs. (A10) and (A12) is replaced by a sum over R. Moreover, this sum is only taken in the interval $0 < R < R_{\max}$, where $R_{\max}$ is the maximum radius for our tabulated surface density.

We have chosen to use the triangle function when computing our potentials, although no large difference was found using the top hat function.

References

Athanassoula E., 1992, MNRAS 259, 328 and 345
Athanassoula E., 1994, In: Shlosman I. (ed.) Mass Transfer induced Activity in Galaxies, Cambridge University Press, Cambridge, p. 143
Ball R., 1992, ApJ 395, 418
Binney J., Tremaine S., 1987, Galactic Dynamics, Princeton University Press
Burstein D., 1979, ApJS 41, 435
Combes F., Sanders R. H., 1981, A&A 96, 164
Contopoulos G., Papayannopoulos Th., 1980, A&A 92, 33
Contopoulos G., Gottesman S.T., Hunter J.H., England M.N., 1989, ApJ 343, 608
Cowie L.L., 1980, ApJ 236, 868
de Vaucouleurs G., de Vaucouleurs A., Corwin H.G., Jr.: 1976, Second Reference Catalogue of Bright Galaxies, Univ. Texas Press 1980
Duval M.F., Athanassoula E., 1983, A&A 121, 297
Elmegreen B.G., Elmegreen D.M., 1985, ApJ 288, 438
England M.N., 1989, ApJ 344, 669
England M.N., Gottesman S.T., Hunter J.H., 1990, ApJ 348, 456
Friedli D., 1994, In: Shlosman I. (ed.) Mass Transfer induced Activity in Galaxies, Cambridge University Press, Cambridge, p. 268
Friedli D., Benz W., 1993, A&A 268, 65
Friedli D., Benz W., 1995, A&A 301, 649
Frogel J.A., Davies R.L., DePoy D.L., Kuchinski L.E., Pogge R.W., Quillen A.C., Ramirez S.V., Sellgren K., Terndrup D.M., Tiede G. 1995, in preparation
Hasan H., Norman C., 1990, ApJ 361, 69
Hjelm M., Lindblad P.O., 1995, A&A accepted
Hockney R.W., Hohl F., 1969, AJ 74, 1102
Hunter J.H., Ball R., Huntley J.M., England M.N., Gottesman S.T. 1988, ApJ 324, 721
Huntley J.M., Sanders R.H., Roberts W.W., 1978, ApJ 221, 521
Jones J.E., Jones B.J.T., 1980, MNRAS 191, 685
Jörsäter S., 1984, Ph.D Thesis Stockholm university
Jörsäter S., van Moorsel G., 1995, AJ 110, 2037 (JvM)
Jörsäter, S., Peterson, C.J., Lindblad, P.O., Boksenberg, A., 1984, A&AS 58,507
Kent S. M., 1987, AJ 93, 1062
Lindblad P.O., Lindblad, P.A.B., 1994, In: King I. R. (ed.) Astronomical Society of the Pacific Conference series 66, The Gaseous and Stellar Disks of the Galaxy, p. 29 (LL94)
Lindblad P.O., Hjelm M., Högbom J., Jörsäter S., Lindblad P.A.B., Santos-Lleó M., 1996, A&A, submitted (L96)
Lindblad P.A.B., Kristen H., 1996, A&A, in preparation
Little B., Carlberg R.G., 1991, MNRAS 250, 161
Miller R.H., Prendergast K.H., 1968, ApJ 151, 699
Quillen A.C., Frogel J.A., González R.A., 1994, ApJ 437, 162
Quillen A.C., Frogel J.A., Kuchinski L.E., Terndrup D.M. 1995, AJ 110, 156
Roberts W.W., Huntley J.M., van Albada G.D., 1979, ApJ 233, 67
Sanders R.H., Huntley J.M., 1976, ApJ 209, 53
Sanders R.H., Tubbs A.D., 1980, ApJ 235, 803
Sandqvist Aa., Jörsäter S., Lindblad P.O., 1982, A&A 110, 336
Sandqvist Aa., Jörsäter S., Lindblad P.O., 1995, A&A 295, 585
Sellwood J.A., 1981, A&A 99, 362
Sellwood J.A., Sparke L.S., 1988, MNRAS 231, 25
Sellwood J.A., Wilkinson A., 1993, Rep. Prog. Phys. 56, 173
Sempere M.J., García-Burillo S., Combes F., Knapen J.H., 1995a, A&A 296, 45
Sempere M.J., Combes F., Casoli F., 1995b, A&A 299, 371
Sørensen S.A., Matsuda T., Fujimoto M., 1976, Ap&SS 43, 491
Sparke L.S., Sellwood J.A., 1987, MNRAS 225, 653
Sygnet J.F., Tagger M., Athanassoula E., Pellat R., 1988, MNRAS 232, 733
Tagger M., Sygnet J.F., Athanassoula E., Pellat R., 1987, ApJ 318, L43
Teuben P.J., Sanders R.H., Atherton P.D., van Albada G.D., 1986, MNRAS 221, 1
Tremaine S., Weinberg M.D., 1984, ApJ 282, L5
Tsikoudi V., 1980, ApJS 43, 365
van Albada G.D., 1985, A&A 142, 491
van Albada G.D., Roberts W.W., 1981, ApJ 246, 740
van Albada G.D., van Leer B., Roberts, Jr. W.W., 1982, A&A 108, 76
Wada K., 1994, PASJ 46, 165
Wada K., Habe A., 1992, MNRAS 258, 82
Wright R.R, 1969, PASP 81, 51

This article was processed by the author using Springer-Verlag LaTeX A&A style file version 3.